

LEVEL

2

NAVAL POSTGRADUATE SCHOOL
Monterey, California

AD A104118



SEP 14 1981
H

THESIS

AN INVESTIGATION OF PARTICULATE BEHAVIOR
IN SOLID PROPELLANT ROCKET MOTORS

by

Stavros George Karagounis

June 1981

Thesis Advisor:

D. W. NETZER

Approved for public release; distribution unlimited

FILE COPY

81 9 11 011

UNCLASSIFIED

SECURITY CLASSIFICATION OF THIS PAGE (When Data Entered)

REPORT DOCUMENTATION PAGE		READ INSTRUCTIONS BEFORE COMPLETING FORM
1. REPORT NUMBER	2. GOVT ACCESSION NO. AD-A104	3. RECIPIENT'S CATALOG NUMBER 118 7
4. TITLE (and Subtitle) An Investigation of Particulate Behavior in Solid Rocket Motors		5. TYPE OF REPORT & PERIOD COVERED (Engineer's Thesis June 1981)
		6. PERFORMING ORG. REPORT NUMBER
7. AUTHOR(s) Stavros George/Karagounis		8. CONTRACT OR GRANT NUMBER(s) MIPR# FO4611-80-X-0032
9. PERFORMING ORGANIZATION NAME AND ADDRESS Naval Postgraduate School Monterey, California		10. PROGRAM ELEMENT, PROJECT, TASK AREA & WORK UNIT NUMBERS 11K
11. CONTROLLING OFFICE NAME AND ADDRESS Air Force Rocket Propulsion Laboratory Edwards, California		12. REPORT DATE June 1981
		13. NUMBER OF PAGES 107
14. MONITORING AGENCY NAME & ADDRESS (if different from Controlling Office)		15. SECURITY CLASS. (of this report) Unclassified
		15a. DECLASSIFICATION/DOWNGRADING SCHEDULE
16. DISTRIBUTION STATEMENT (of this Report) Approved for public release; distribution unlimited.		
17. DISTRIBUTION STATEMENT (of the abstract entered in Block 20, if different from Report)		
18. SUPPLEMENTARY NOTES		
19. KEY WORDS (Continue on reverse side if necessary and identify by block number) Solid Rocket Motors High-Speed Cinematography Metallized Propellants Holography Light Scattering		
20. ABSTRACT (Continue on reverse side if necessary and identify by block number) An apparatus was developed which used diffractively-scattered laser power spectra measurements for determination of exhaust particulate size from solid rocket motors. The apparatus was calibrated by using glass beads and aluminum oxide powder, and then used with success to estimate the mean diameter of the exhaust particles of a small solid rocket motor. Scanning electron microscope measurements of the exhaust particles were employed for comparison and verification.		

DD FORM 1473

1 JAN 73

EDITION OF 1 NOV 68 IS OBSOLETE
S/N 0102-010-6001

UNCLASSIFIED

SECURITY CLASSIFICATION OF THIS PAGE (When Data Entered)

UNCLASSIFIED

SECURITY CLASSIFICATION OF THIS PAGE/When Data Entered

Holographic pictures from burning propellant strands and slabs of different compositions were obtained at different pressures and compared to corresponding high speed, high resolution motion pictures.

Accession For	
NTIS GRA&I	<input checked="checked" type="checkbox"/>
DTIC TAB	<input type="checkbox"/>
Unannounced	<input type="checkbox"/>
Justification	<input type="checkbox"/>
By _____	
Distribution/	
Availability Codes	
Dist _____	
Special	
A	

DD Form 1473
Jan 73
S/N 0102-014-6601

UNCLASSIFIED

SECURITY CLASSIFICATION OF THIS PAGE/When Data Entered

Approved for public release; distribution unlimited

An Investigation of Particulate Behavior
in Solid Rocket Motors

by

Stavros George Karagounis
Major, Hellenic Air Force
B.S., Naval Postgraduate School, 1980
M.S., Naval Postgraduate School, 1980

Submitted in partial fulfillment of the
requirements for the degree of

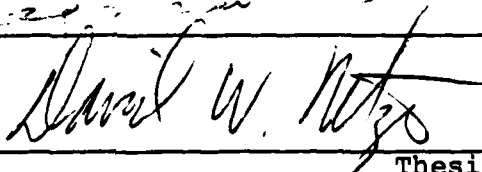
AERONAUTICAL ENGINEER

from the

NAVAL POSTGRADUATE SCHOOL
June 1981

Author

Approved by:



Thesis Advisor



Second Reader


Chairman, Department of Aeronautics



Dean of Science and Engineering

ABSTRACT

An apparatus was developed which used diffractively-scattered laser power spectra measurements for determination of exhaust particulate size from solid rocket motors. The apparatus was calibrated by using glass beads and aluminum oxide powder, and then used with success to estimate the mean diameter of the exhaust particles of a small solid rocket motor. Scanning electron microscope measurements of the exhaust particles were employed for comparison and verification.

Holographic pictures from burning propellant strands and slabs of different compositions were obtained at different pressures and compared to corresponding high speed, high resolution motion pictures.

TABLE OF CONTENTS

	Page
I. INTRODUCTION -----	10
II. METHOD OF INVESTIGATION -----	19
III. HIGH-SPEED CINEMATOGRAPHY INVESTIGATION -----	20
A. INTRODUCTION -----	20
B. EXPERIMENTAL APPARATUS -----	21
C. EXPERIMENTAL PROCEDURES -----	23
D. RESULTS AND DISCUSSION -----	23
IV. DIFFRACTIVELY SCATTERED LIGHT METHOD -----	36
A. THEORETICAL CONSIDERATIONS -----	36
1. Introduction -----	36
2. Forward Scattering Ratio Technique ----	37
3. Applicability of Forward-Scattering Ratio Technique to Al_2O_3 and Al Particles -----	41
B. OPTICAL ARRANGEMENT -----	45
C. EXPERIMENTAL PROCEDURE -----	47
D. DISCUSSION OF RESULTS -----	56
V. HOLOGRAPHIC METHOD -----	72
A. INTRODUCTION -----	72
B. EXPERIMENTAL APPARATUS -----	74
C. EXPERIMENTAL PROCEDURE -----	77
D. RESULTS AND DISCUSSION -----	79
VI. CONCLUSIONS AND RECOMMENDATIONS -----	83
LIST OF REFERENCES -----	102
INITIAL DISTRIBUTION LIST -----	107

LIST OF TABLES

Table	Page
I. PROPELLANT COMPOSITIONS -----	25
II. HIGH SPEED MOTION PICTURE TEST CONDITIONS (REF. 17) -----	26
III. EXPERIMENTAL APPARATUS FOR DSL METHOD -----	59
IV. VOLUME-SURFACE MEAN DIAMETER (D_{32}) MEASUREMENT RESULTS -----	60

LIST OF FIGURES

Figure	Page
1. Photograph of Combustion Bomb (a) Experimental Set-up, (b) Modified Window -----	28
2. Schematic of Combustion Bomb Modification -----	29
3. Schematic of Combustion Bomb -----	30
4. Circuit Diagram of Remote Control Panel -----	31
5. Schematic of Experimental Apparatus -----	32
6. Focal Distance (Lens to Object) Versus Extension Tube Length -----	33
7. Photograph of Camera Mount Improvement-Expansion Screws -----	34
8. Photographs of 1951 USAF Resolution Target (a) Ref. 17, (b) present work -----	35
9. Nondimensionalized Illumination Profiles [I(θ) versus θ] -----	61
10. Schematic Diagram of Diffractively Scattered Light Apparatus -----	62
11. Photographs of Light Scattering Set-up -----	63
12. Photodiode Output Voltage versus Distance from Centerline for Glass Beads -----	64
13. Light Scattering Geometry -----	65
14. Photodiode Output Voltage versus Distance from Centerline for Al ₂ O ₃ Particles -----	66
15. Photodiode Output-Voltage Profiles versus Distance from Optical Centerline (actual runs) ---	67
16. SEM Photomicrographs of Rocket Exhaust Particles (clean) -----	68
17. SEM Photomicrographs of Rocket Exhaust Particles (as-collected) -----	69
18. Size Distribution of Clean Exhaust Particles from Propellant MWC-1, Burned at 190 psi -----	70

	Page
19. Size Distribution-of (As-Collected) Exhaust Particles from Propellant NWC-1, burned at 190 psi -----	71
20. Sketch of RPL Holocamera -----	85
21. Schematic of Two-beam Lens-assisted Holographic Arrangement (Adapted from Ref. 45) -----	86
22. Schematic of Hologram Reconstruction Method (Adapted from Ref. 45) -----	87
23. Photographs of RPL Ruby Laser Components -----	88
24. Photograph of the Hologram Reconstruction Apparatus -----	89
25. Photograph of 2-D Motor with Control Box and Holocamera -----	90
26. Photograph of 2-D Motor Components -----	90
27. Schematic of 2-D Motor Holographic Apparatus ----	91
28. Hologram of 1951 USAF Resolution Target -----	92
29. WGS-5A Propellant Burned at 500 psi -----	93
30. WGS-5A Propellant Burned at 1000 psi -----	94
31. WGS-6A Propellant Burned at 500 psi -----	95
32. WGS-6A Propellant Burned at 1000 psi -----	96
33. WGS-7A Propellant Burned at 500 psi -----	97
34. WGS-7A Propellant Burned at 1000 psi -----	98
35. N-7 Propellant Holograms 50 μ sec Pulse -----	99
36. WGS-7 Propellant Burned at 1000 psi -----	100
37. Hologram of WGS-5A Propellant Burned at Atmospheric Pressure, 10 μ sec pulse, No ND Filter: Scale 1443 μ m/in -----	101

ACKNOWLEDGMENT

In addition to my appreciation for the patience of my wife and children and their willingness to share myself with this study, I would like to acknowledge the advice and assistance provided by Professor D. W. Netzer whose high sense of professionalism was a great inspiration for me. Appreciation is also expressed to Mr. P. J. Hickey, Aerospace Engineering Technician. Without his exceptional skills this work would have been much more difficult to me.

I. INTRODUCTION

Metal additives can significantly increase the theoretical and deliverable specific impulse of solid propellant rocket motors. However, compared to other solid rocket propellant ingredients, they can often hinder the achievement of complete combustion and may cause significant two-phase flow losses. They may be difficult to vaporize and ignite, slow to burn, and may form condensed reaction products of even higher mass and density than the original metals. The presence of solid (or liquid) particles in the gas flow results in a slowing down of the gas flow, and more particularly in reducing the exhaust velocity, which is proportional to the thrust and specific impulse. This reduction increases almost linearly with the mass of unburned solid or liquid particles contained per unit mass of the combustion products. It has been shown that the equilibrium state for temperatures and velocities is approximately reached when the diameter of the particles is smaller than 10^{-3} to 10^{-4} cm [Ref. 1]. However, the presence of condensed products of any size in the flow reduces the efficiency by which the thermal energy is transformed into kinetic energy in the nozzle. Performance loss estimates indicate that about 1% specific impulse is lost for each 10% of unburned aluminum. Two-phase flow losses, e.g., of 2-10% specific impulse, are associated with the presence of Al_2O_3 in the flow with the larger losses occurring with

motors that have smaller nozzle throat diameter [Ref.]. The fate of partially unburned metal droplets which enter the nozzle flow field is uncertain. It is believed that they may fragment and react to a significant degree downstream of the throat, thereby permitting the late recovery of some of their combustion energy by the exhaust stream [Ref. 2].

The original metal particles added to solid propellants may ignite and leave the surface immediately or form agglomerates, which may contain hundreds or even thousands of the original particles. In general, smaller agglomerate masses lead to higher combustion efficiencies, less slag retention and lower two-phase flow losses as the combustion products accelerate through the rocket nozzle. It has been found [Ref. 2] that the metallic species leaving the grain and entering the nozzle consists of a mixture of the original metal (e.g. Al) and its oxides (e.g. Al_2O_3 , AlO and Al_2O), with a broad size distribution. The oxides may range from submicron to 30 micron, while unburned metal droplets may range to several hundred microns.

Conclusions with respect to agglomerate size, combustion efficiency and slag formation are strongly dependent on the propellant type and the motor geometry. However, analysis of size distributions of the agglomerates leaving the surface has revealed that the following parameters decrease with increasing pressure [Ref. 3]: Collision

frequency on the burning surface, agglomerate stay time on the surface, and mean agglomerate size. Increasing the cross-flow velocity decreases the mean agglomerate size but chamber pressure, apparently, has the most pronounced effect on agglomerate size. Propellants containing large aluminum particles (e.g. 50 vs 6 μm) have also been found to burn without the aluminum igniting or agglomerating on the surface [Ref. 3].

Predictions of performance losses due to the presence of Al_2O_3 , mentioned above, are very sensitive to the aluminum oxide particle size distribution, and no direct experimental data are available as a function of the position along the nozzle. The only data available has come from the residues from small propellant samples burned in closed combustion bombs or from particle collection external to the exit plane of a motor.

Two different approaches have been used to incorporate two phase flow losses into motor efficiency predictions. The first involves correlating experimental particle size data with motor and propellant variables, as in the original SPP effort [Ref. 4]. The second approach involves calculating the exhaust particle size based on a critical Weber number [Ref. 5]. A maximum droplet size criteria is used, which states that the size of the droplets entering the high acceleration field of the nozzle inlet and throat will be reduced to the maximum size permitted by the tradeoff

between droplet surface tension and the shear forces created by the acceleration. While this method accounts for the maximum size, it says nothing about the mass ratio of the large particles to the less-than-two-microns particles which are also present. The bias in collection techniques and devices have resulted in opinions ranging from the exhaust particles being nearly all-fine to the all-coarse extreme [Ref. 5]. In any event, it is possible that combustion processes which result in chamber products smaller than the maximum stable diameter in the nozzle result in significant motor performance gains.

Very little experimental data are available which can be used to determine the effects of such parameters as binder composition, initial aluminum size and weight percentage, and oxidizer size on the two phase flow losses [Refs. 3, 6 - 12]. Several existing performance analysis programs model the important processes of momentum and energy exchange between the solid, liquid and the gaseous phases, but none accounts for particle or droplet size changes in any realistic manner. These omissions can result in considerable error in the prediction of two-phase flow performance losses. A very complete survey of recent advances in solid rocket motor performance prediction capability is presented in Ref. 13.

Propellant combustion models have improved considerably over the last five years but all of them are weak and/or

invalidated, when metals are included in the propellant [Refs. 14 & 15]. These models make various assumptions concerning the relationship between the particle sizes in the gas phase and the aluminum size in the propellant. Aluminum particle melting, ignition and combustion, and the subsequent heat release and heat transfer back to the burning propellant surface should be accounted for in these models [Refs. 5, 15 & 16].

The drawbacks resulting from adding metals to solid rocket propellants are balanced by the high combustion energy of metals and the reduction of H_2O and CO_2 to lower molecular weight gases during burning, leading to a net advantage in many applications where exhaust smoke can be tolerated.

Another reason solids like Al and Al_2O_3 are added to a solid rocket motor is to dampen combustion pressure oscillations. The desired range of agglomerate mass and size required to defeat a particular mode of acoustic instability is very dependent on the frequencies of the undesired oscillations. Thus, control and knowledge of agglomerate size is often an important consideration in propellant and rocket motor development programs.

A research project entitled "Solid Propellant Combustion" was initially funded by the Naval Postgraduate School Foundation Research Program and subsequently by Air Force Rocket Propulsion Laboratory (AFRPL), Edwards, California.

The overall goal of this research is to relate propellant composition and operating environment to the behavior of solid (Al, Al_2O_3) within the grain port and exhaust nozzle.

The initial effort at the Naval Postgraduate School (NPS) is directed at obtaining detailed experimental data on the effects of initial aluminum size and operating pressure on the particulate characteristics within the gas phase. To that purpose four experimental techniques were chosen:

a. High speed cinematography for the observation of strand burners within a combustion bomb and a 2-D slab motor under different operating pressures.

b. Post-fire residue collection and examination with a scanning electron microscope (SEM).

c. Scattered laser power spectra measurements to determine the mean diameter and concentration of particles as they vary through the exhaust nozzle.

d. Holographic observation of the combustion process of burning propellant strands and of burning propellant slabs in a cross-flow environment, using a 2-D, windowed motor.

The data obtained with varying initial Al size and operating pressure can be used to validate some of the basic assumptions employed in current combustion/performance prediction models. In applying all four of the above techniques, relative advantages and disadvantages of each

technique (resolution, etc.) for obtaining these data need to be determined.

Diloreto [Ref. 17] has conducted an initial investigation of six specially formulated propellants using high speed motion pictures and SEM examination of post-fire residue from propellant strands burned in a combustion bomb.

There are some known advantages and disadvantages for each of the above techniques. By using high speed motion pictures of burning strands, the entire duration of the burning process can be recorded to provide data concerning the time-varying characteristics. In addition, the combustion pressure can be independently varied using a combustion bomb and the collection of post-fire residue is readily made. These tests are relatively easily conducted and inexpensive. There is one major disadvantage of using propellant strands; the different burning environment in comparison with the actual one in a rocket motor. Thus, (a) there is no cross-flow over the burning surface and (b) burning agglomerates are quenched in the cold inert gas used to pressurize the bomb. In addition, the heat transfer to the burning surface and the related burning rate have been found to depend upon the dimensions of the propellant strand and those of the combustion bomb. The size of the flame envelope around the burning particles is also a function of pressure and propellant composition. The latter often prevents actual particle sizes from being obtained from the motion pictures.

Other disadvantages of high speed cinematography include the image resolution limitations due to the optics employed and the film used, as well as due to the smoke and/or a high number-concentration of particles above the burning surface. In addition, the depth of field is critically limited if any appreciable magnification is employed. Concluding, the combustion bomb technique and the associated cinephotomicrography are good tools for comparing burning surface details for different propellants, as well as for observing the macro-structure of the luminous flames [Ref. 7].

Measuring the scattered laser power spectra from an aerosol is a well known method for obtaining the mean particle size and particles concentration without interfering with the flow. Application of the technique has had only limited success in practical combustion environments. A disadvantage of this method is that it can be used to determine only the mean diameter and not the size distribution of the particles. Hermesen also indicates that the technique is biased towards small particles [Ref. 5]. One major advantage is that the technique is not significantly hindered by high velocity environments.

The main advantages of the holographic methods are (a) resolution to less than 10 μm with the particle-surrounding flames eliminated by the use of narrow pass filters and (b) unique depth of field [Ref. 18].

Utilization of a two-dimensional slab motor with this method also provides a realistic combustion environment. In the disadvantages of this technique one would include that it yields just one or two instants of the combustion history. A major current disadvantage also lies in the time required for reduction of the data available in the hologram.

The scope of the present investigation was (a) to compare holographic and motion picture data from burning propellant strands, and (b) to develop and calibrate a diffractively-scattered laser power apparatus and apply the technique to the exhaust products from a small rocket motor.

II. METHOD OF INVESTIGATION

An effort was placed in improving the resolution of the motion pictures taken by Diloreto [Ref. 17] by modifying the combustion bomb and camera optics.

Holographic pictures from burning propellant strands of different composition were obtained at different pressures and compared to corresponding motion pictures.

An apparatus was developed for applying the diffractively-scattered laser power spectra technique for particle size determination. The apparatus was calibrated by using glass beads and aluminum-oxide powder, and then used to estimate the mean diameter of the exhaust particles from a small solid rocket motor. Scanning electron microscope measurements of the exhaust particles were employed for comparison and verification.

III. HIGH-SPEED CINEMATOGRAPHY INVESTIGATION

A. INTRODUCTION

A series of combustion bomb tests were conducted at NPS by Diloreto [Ref. 17]. Propellant strands were burned in an inert gas environment at 500 and 1000 psi. A windowed combustion bomb permitted high-speed motion picture analysis of the burning propellant strands. Four aluminized (5% by weight) propellants and two propellants with aluminum oxide (.5% and 1%) were investigated and post-fire particle residues were analyzed with a scanning electron microscope and found to have bi-modal size distributions. The mean diameter of the coarse particles was approximately the same size as the initial aluminum cast in the propellant. Measurements taken from the high-speed motion pictures included resolution, propellant burning rate, the diameter of burning particles ejected from the surface, and the vertical velocity of these particles. The diameters of the flame envelopes around the burning particles were found to be approximately 7 to 12 times the diameter of the initial aluminum cast in the propellant. The oxidizer-rich environment of the aluminized propellants resulted in the aluminum leaving the surface immediately (without agglomeration) and a very large burning vapor envelope. A resolution of 70 μm was obtained using a magnification of 0.70 on the film, at 5000 frames per second. It was also observed that the velocity of any particular burning particle was nearly constant

above the surface, once it departed the region very near the burning surface. Smaller particles travelled at higher velocities, as expected. Finally, it was found that propellant burning rates were approximately constant at a given pressure with only a slight increase for propellants with smaller initial aluminum size. Burning rates at 1000 psi were approximately 17% higher than at 500 psi.

Propellant compositions and the test conditions for the motion pictures taken by Diloreto [Ref. 17] are presented in Tables I and II, respectively.

In the above work it was noticed that, when the camera was focused on the resolution target, the maximum resolution through the camera optics was 15 μm vs 70 μm on the developed film. This difference was attributed to the limiting resolution of the film and/or to camera vibrations.

The aim of the present work was to improve the obtainable resolution. To this end three modifications were evaluated; (a) increased magnification on the film plane by using longer extension tubes on the camera, (b) a thinner optical-quality viewing window, and (c) increased stability of the camera mounting.

B. EXPERIMENTAL APPARATUS

The combustion bomb used in this investigation was a two piece unit made from 347 stainless steel (Fig. 1). It had a core volume of about 34 cubic inches and an inside diameter of 2 inches. The existing bomb [Ref. 17] was

modified to allow for the placement of the objective lens of the camera closer to the propellant strand by means of extension tubes. The thickness of the bomb wall was reduced to 1 inch in the area of the window facing the camera. The existing optical quality glass window of 1 inch thickness was replaced with one of 0.500 inch thickness and 0.75 inch diameter. Details of the bomb modification are shown in Figure 2, while a schematic of the entire bomb is presented in Figure 3. The modification reduced the maximum allowable working pressure to 1500 psi. Two other windows, each one inch in diameter and one inch in thickness were incorporated in the bomb, one diametrically opposite to the viewing window and one located 90 degrees between the first two. These windows were used for back and side lighting of the propellant strands.

Pressurization of the combustion bomb, ignition of the propellant strands, and activation of the high speed camera were controlled from a remote control panel located in a safety booth situated out of the line of sight of the combustion bomb windows. Figure 4 is a circuit diagram of the remote control installation. A schematic of the experimental apparatus is shown in Figure 5.

Several extension tubes were fabricated for the Hycam camera in order to increase the magnification on the film plane. An f1:9 lens was used on the end of the extension tube. Figure 6 presents the focal distance (lens to

object) as a function of extension tube length. The camera mounts were also improved by incorporation expansion screws between the frame and mounting table as shown in Figure 7.

C. EXPERIMENTAL PROCEDURES

Details of the experimental procedures are presented in Ref. 17. In this investigation, several films were taken of the 1951 USAF resolution target with the system modified as discussed above. After acceptable resolution and magnification were obtained within the constraints of the modified camera and combustion bomb, a motion picture was taken of propellant WGS-7A burning at 500 psi.

D. RESULTS AND DISCUSSION

The longer (2.75 inch) extension tube which was finally used on the camera along with the combustion bomb modification, and the camera mounts improvement led to a 1.12X magnification on the film versus 0.7X reported in Ref. 17. The resolution was also considerably improved to about 14 μ from 70 μ reported in the above reference. Two pictures of the 1951 USAF Resolution Target are presented in Figure 8 for comparison, where (a) came from Ref. 17 and (b) from the present work. The motion picture of propellant WGS-7A burning at 500 psi obtained in Ref. 17 was compared to the one from this work. Better detail was observed in the new film, but significantly better data could not be obtained since the flame envelopes still shielded the

the particles. These envelopes could possibly be minimized on the film if monochromatic illumination were used with appropriate narrow pass filters.

There is no doubt that both high resolution and reasonable magnification on the film are quite desirable features in propellant burning investigations by high-speed cinematography. However, the higher the values of these parameters the less the depth of field and, therefore, the lower the number of observable particulates in sharp focus. For best results a compromise must be made between resolution and depth of field. Also, since the optics involved play a critical role in the image quality and especially in the resolution, appropriate care should be taken to use high quality optics.

TABLE I
PROPELLANT COMPOSITIONS
(Ref. 17)

Propellant Designation	Binder % Weight	Oxidizer % Weight	Metal % Weight	Mean Metal Diameter, μm
WGS-5A	HTPB 12	AP 83	Al 5	75-88
WGS-6A	HTPB 12	AP 83	Al 5	45-62
WGS-7A	HTPB 12	AP 83	Al 5	23-27
WGS-7	HTPB 12	AP 83	Al 5	7-8
NWC-1 ¹	HTPB 12	AP 87	Al ₂ O ₃ 1.0	8
NWC-2 ¹	HTPB 12	AP 87.5	Al ₂ O ₃ 0.5	8
N-7	PBAN 18	AP 67.0	Al 15	44

Note:

1. Approximate formulation

TABLE II
HIGH SPEED MOTION PICTURE TEST CONDITIONS
(Ref. 17)

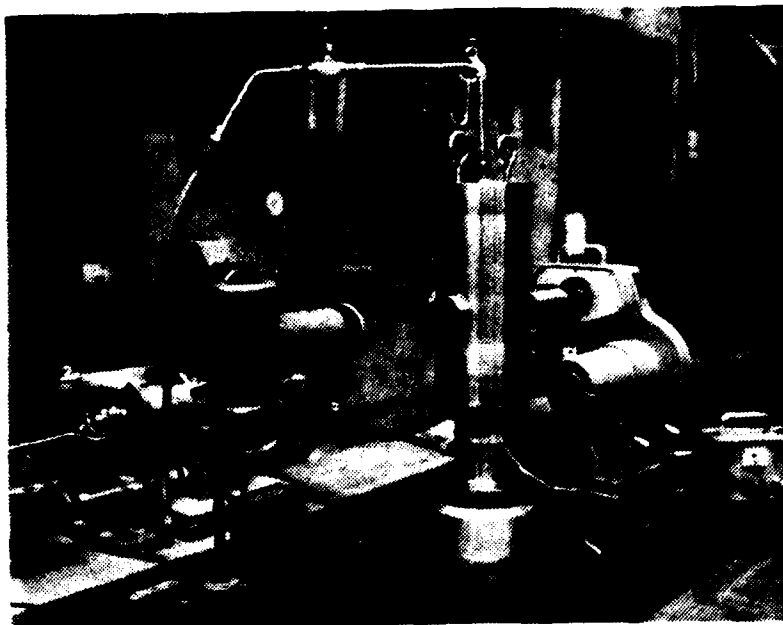
Test Number	Propellant Type	Pressure PSI	Film Type	f/STOP	EXTERNAL LIGHT
1545050480	WGS-5A	500	EKTACHROME 7250	4.0	650 W SIDE
1600260480	WGS-5A	500	KODACHROME 25	1.9	1200 W SIDE 650 W BACK
1500300480	WGS-5A	1000	KODACHROME 25	1.9	1200 W SIDE 650 W BACK
1415010580	WGS-6A	500	KODACHROME 25	1.9	1200 W SIDE 650 W BACK
1415250580	WGS-6A	500	KODACHROME 25	1.9	1200 W SIDE 650 W BACK
1315010580	WGS-6A	1000	KODACHROME 25	1.9	1200 W SIDE 650 W BACK
1100250580	WGS-6A	1000	KODACHROME 25	1.9	1200 W SIDE 650 W BACK
1300250580	WGS-7A	500	EKTACHROME 7250	5.6	1200 W SIDE 650 W BACK
1700300480	WGS-7A	1000	KODACHROME 25	1.9	1200 W SIDE 650 W BACK
1345250580	WGS-7	500	KODACHROME 25	1.9	1200 W SIDE 650 W BACK

TABLE II
(continued)

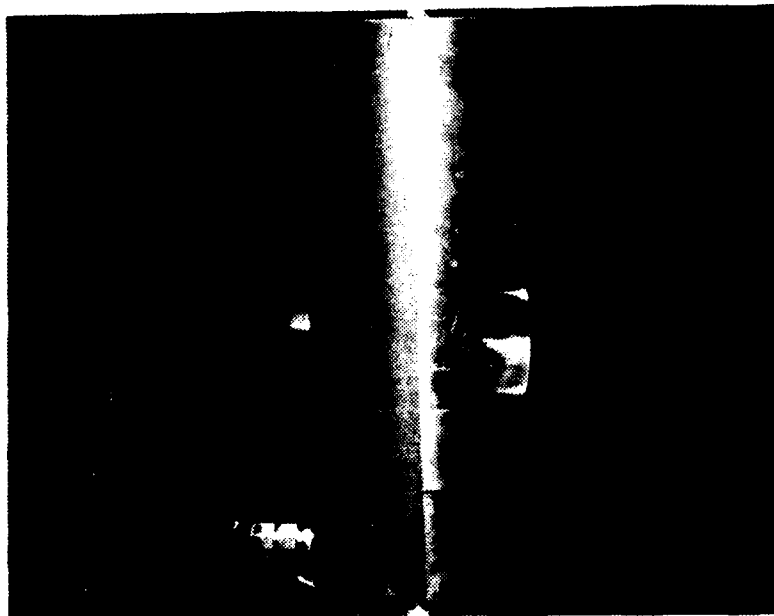
Test Number	Propellant Type	Pressure PSI	Film Type	f/STOP	EXTERNAL LIGHT
1615300480	WGS-7	1000	KODACHROME 25	1.9	1200 W SIDE 650 W BACK
1500250580	NWC-1	500	KODACHROME 25	1.9	1200 W SIDE 650 W BACK
1145250580	NWC-1	1000	KODACHROME 25	1.9	1200 W SIDE 650 W BACK
1530250580	NWC-2	500	KODACHROME 25	1.9	1200 W SIDE 650 W BACK
1215250580	NWC-2	1000	KODACHROME 25	1.9	1200 W SIDE 650 W BACK

Note:

1. The Frame rate for all tests was 5000 pictures per second.



a. Experimental Set-up



b. Modified Window

Fig. 1. Photograph of Combustion Bomb

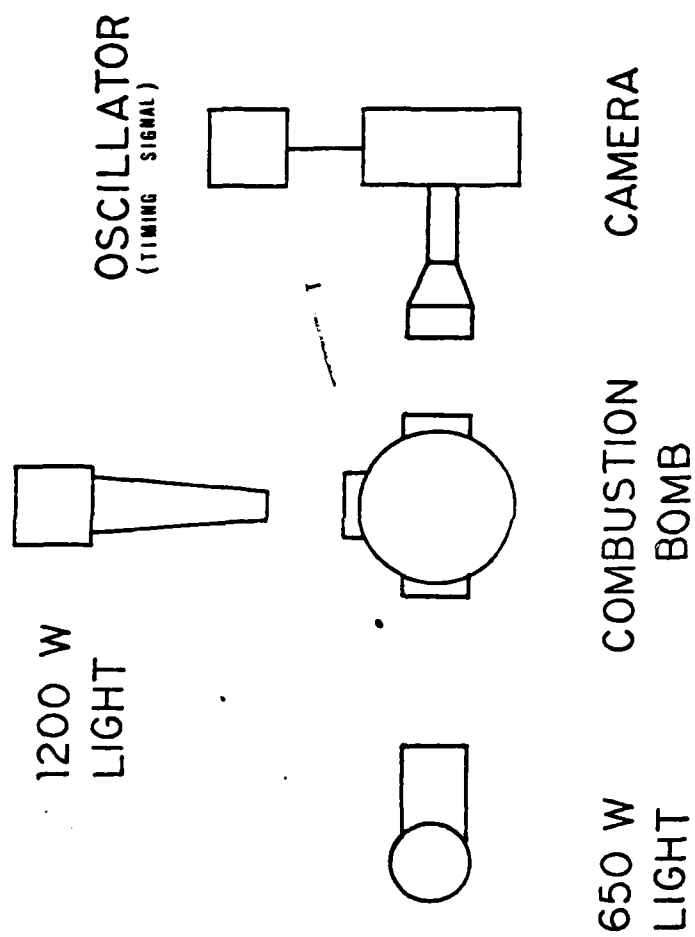


Fig. 5. Schematic of Experimental Apparatus
(Ref. 17)

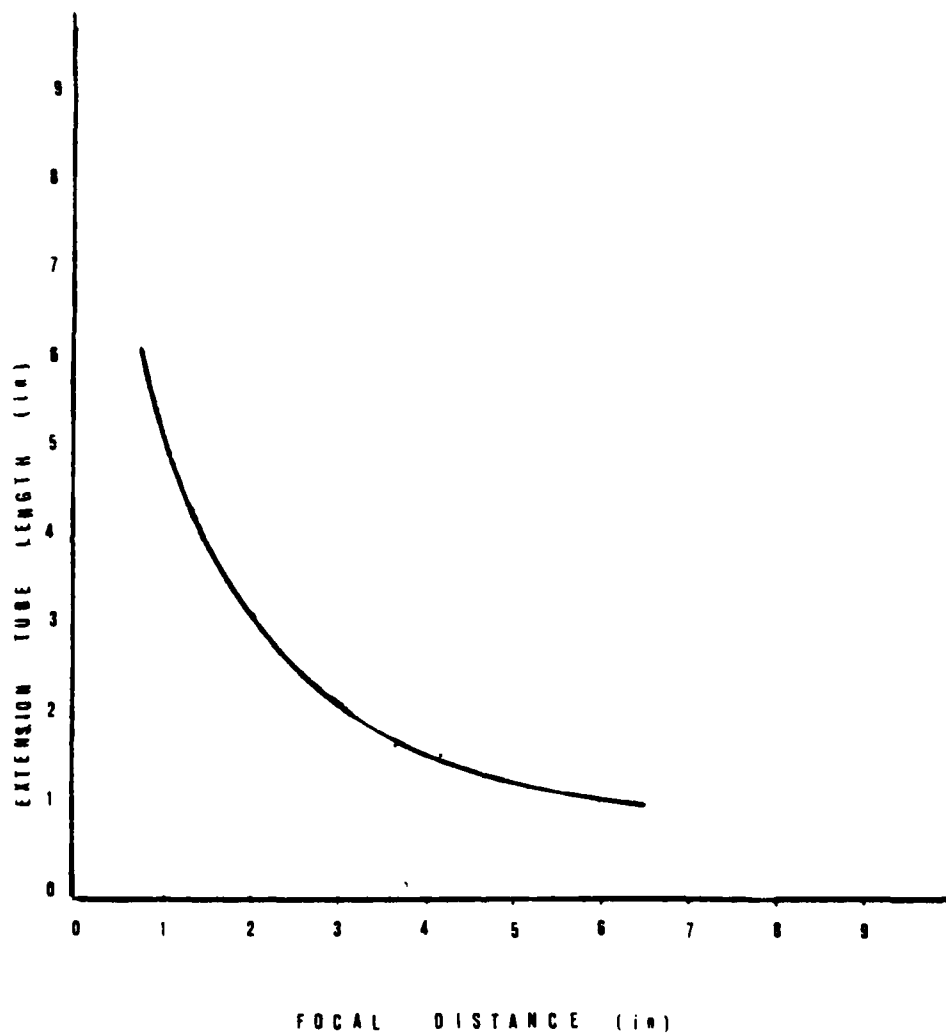


Fig. 6. Focal Distance (lens to object)
versus Extension Tube Length

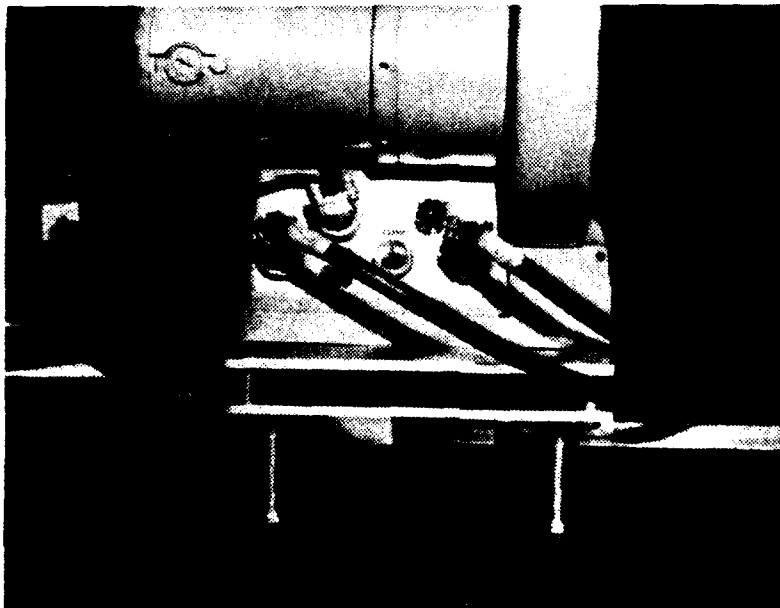
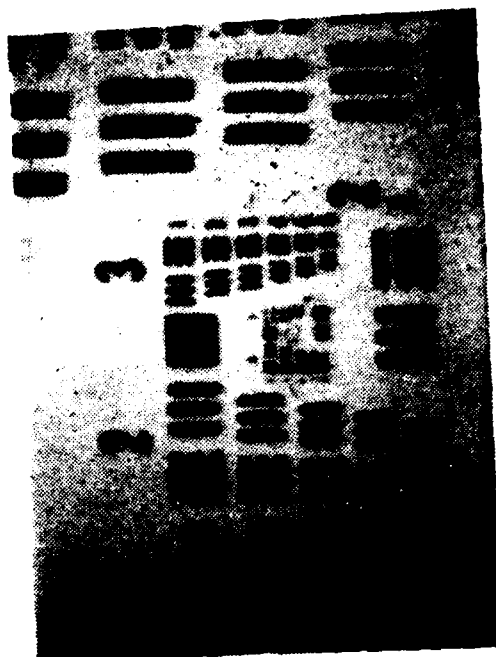


Fig. 7. Photograph of Camera Mount Improvement -
Expansion Screws



b. Present Work

a. Ref. 17

Fig. 8. Photographs of 1951 USAF Resolution Target

IV. DIFFRACTIVELY SCATTERED LIGHT METHOD

A. THEORETICAL CONSIDERATION

1. Introduction

Based on a theory by Gumprecht and Sliepeevich [Ref. 21], describing the scattering properties of a polydispersion, an investigation of the light scattering technique was first conducted by Chin, Sliepeevich and Tribus [Ref. 22]. A more generalized theory on the same subject was later discussed by Dobbins, Crocco, and Glassman [Ref. 23], though applicable only to certain types of drop-let size distributions. After the introduction of the "upper-limit distribution function" (ULDF) by Mugels and Evans [Ref. 24], Roberts and Webb [Ref. 25] concluded that the volume - surface mean diameter D_{32} of a polydispersion may be determined from the intensity of diffractively scattered light from spherical particles. This could be done with a good degree of accuracy without any knowledge of the general distribution type. Dobbins and Jizmagian [Refs. 26 & 27] also concluded that the mean scattering cross section of particles depends primarily on the mean diameter D_{32} , regardless of the size distribution function, when the refractive index is near unity. Also, Hodkinson [Ref. 28] showed that the ratio of scattered light intensities at two forward angles is relatively insensitive to particle refractive index and concentration, and that this ratio yields a measure of the volume-surface diameter D_{32} .

Based on the above background a method was developed for estimating the volume-surface mean diameter D_{32} of a polydispersion of particles by means of diffractively scattered light intensities. This method has been used by A. S. Nejad, et al [Ref. 16] for measurement of the mean droplet diameter resulting from atomization of a transverse liquid jet in a supersonic air stream as well as by others for particles of different nature. Powell, et al [Ref. 29] used this technique combined with light transmission measurements for the simultaneous estimation of mean diameter, refractive index and volume concentration of aerosols.

Other approaches using scattered and/or transmitted light intensities [e.g. Refs. 30 & 31] have been used for determination of aerosol sizes.

2. Forward Scattering Ratio Technique

The theory for the scattering of light by a single dielectric spherical particle of size number α equal to $\frac{\pi D}{\lambda}$ (where D is the diameter and λ the wavelength of incident light) gives the following expression for the radiant intensity $I(\theta)$ scattered at a small angle θ (in radians) measured from the forward direction [Ref. 23).

$$\frac{I(\theta)}{E_o} = \frac{D^2}{16} \left\{ \alpha^2 \left[\frac{2J_1(\alpha\theta)}{\alpha\theta} \right]^2 + \left[\frac{4m^2}{(m^2-1)(m+1)} \right]^2 + 1 \right\} \quad (1)$$

where E_0 is the irradiance of an incident planar wave, m is the refractive index of the scattering media and J_1 is the Bessel function of the first kind of order unity.

The three terms in the bracket of Equation (1) represent, respectively, the Fraunhofer diffraction, the optical scattering due to refraction of the centrally transmitted ray, and the scattering due to a grazingly incident ray. The following conditions must be met to assure the validity of Equation (1), [Ref. 21.].

- (1) The incident light must be planar.
- (2) The forward angle θ must be small enough so that $\theta \simeq \sin \theta$.
- (3) The particle size number α must be large compared to unity.
- (4) The phase shift, $2\alpha(m-1)$, must be large compared to unity.
- (5) The distance between the particle and the observer (photosensor) must be large compared to D^2/λ .
- (6) The particles must be non-absorbing of light.

If a polydispersion of particles is present, the integral intensity of all particles is found by summing over all diameters present. The relative frequency of occurrence of particles of a given diameter D can be considered to be distributed according to a distribution function $N(D)$. $N(D)$ is defined in such a way that its integral over a given diameter interval equals to the probability of occurrence of particles with diameters within that specific interval.

It has been shown [Ref. 23] that when the expression for the intensity of scattering due to a polydispersion is normalized by dividing by the intensity of diffractively scattered light in the forward direction ($\theta = 0$), the second and third terms in Equation (2) are small and can be ignored. In this case, the normalized, integrated intensity of forward scattered light $I(\theta)$ (at a small angle θ) due to a polydispersion of large (compared to the wavelength) particles is given as

$$I(\theta) = \frac{\int_0^{D_\infty} \left[\frac{2J_1(\alpha\theta)}{\alpha\theta} \right]^2 N(D) D^4 dD}{\int_0^{D_\infty} N(D) D^4 dD} \quad (2)$$

Equation (2) holds when all particles are equally illuminated or, in other words when the attenuation of the incident light is slight.

The transmission law for a polydispersion of particles is given by [Ref. 30].

$$\frac{E}{E_0} = e^{-\tau l} = \exp \left(- \frac{3}{2\rho_p} \bar{Q} C_m \frac{L}{D_{32}} \right) \quad (3)$$

where \bar{Q} is the average extinction coefficient,

C_m is the mass concentration of particles

L is the path length

ρ_p is the density of an individual particle

and D_{32} is the volume-surface mean particle diameter

\bar{Q} and D_{32} are defined as

$$\bar{Q} = \sum Q(D) N(D) D^2 \Delta D / \sum N(D) D^2 \Delta D \quad (4)$$

and

$$D_{32} = \sum N(D) D^3 \Delta D / \sum N(D) D^2 \Delta D \quad (5)$$

where Q the extinction coefficient and is a function of D , λ and m . It has been recommended [Ref. 23] that "the optical depth (τl) be maintained below 1.5 in order to assure absence of adverse distortion of the illumination profile". This recommendation can be translated as

$$\frac{E}{E_0} > 0.223 \quad (6)$$

Roberti and Webb [Ref. 25] have shown that D_{32} may be determined for a polydispersion of particles using equation (2), for a wide range of size distributions. Their work resulted in the determination of a "universal" illumination profile, i.e., the mean curve for the scattered intensity $I(\theta)$ plotted versus a reduced angle of scattering $\pi D_{32} \theta / \lambda$ (where θ is the forward scattering angle and λ the wavelength of the incident light). This "universal" profile is reproduced in Figure 9.

In a practical situation, a value of D_{32} may be determined by using the above method as follows [Ref. 16]:

(1) The optical apparatus is calibrated ($I(\theta)$ vs θ) by using particles of known size as scattering media (i.e., the "closeness of fit" to the "universal" profile is determined).

(2) The actual particles are introduced into the system and $I(\theta)$ is measured as a function of θ . The "universal" curve is then used to determine D_{32} .

(3) Equation (3) can be used to determine the particle concentration C_m .

Most calculations have been made for spherical particles. However, the Fraunhofer-diffraction forward lobe from an assembly of irregular particles in random orientation is similar in shape to the one of spheres [Refs. 32-35] so the same curve should be usable. The necessary correction factor can be applied for some particle shapes [Ref. 28].

3. Applicability of Forward - Scattering - Ratio Technique to Al_2O_3 and Al Particles

For the technique to be applicable in estimating the mean size of the particles coming out of a rocket nozzle, the six conditions for the validity of Equation (2) must be met. These conditions will be discussed here in relation to the experiment conducted.

(1) The requirement for planarity of incident light was satisfied by the use of a He-Ne laser as the light source in conjunction with a spatial filter/beam expander-collimator.

(2) The forward angle θ was kept small ($0 < \theta < 6^\circ$).

(3) The condition calling for large particle size number $\alpha = \frac{\pi D}{\lambda}$ was generally met, since for $\lambda = .6328 \mu\text{m}$, $1 < \alpha < 100$. (The lower limit is imposed by the fact that at $\alpha < 1$ a scattering pattern independent of particle sizes is approached [Ref. 28].)

(4) The phase shift, $\rho = 2\alpha(m-1)$, should also be large.

The refractive index m (or, rather, the real part of it, n_1), has been found to be 1.77 for a wavelength of $0.5 \mu\text{m}$ and 1.75 for $1 \mu\text{m}$ [Ref. 36]. Thus, for the He-Ne laser wavelength of $.6328 \mu\text{m}$, $m = 1.76$ can be safely assumed. Then $1.52 < \rho < 152$ for $.2 < D < 20 \mu\text{m}$. If the typical radius of the Al_2O_3 particles is $.2 \mu\text{m}$ [Ref. 36], the phase shift would be approximately 3, which is satisfactorily large compared with the values found in the bibliography (see Table 1 in [Ref. 28]).

(5) The distance between the light scattering particles and the photosensor was set at approximately $.728 \text{ m}$. This is much greater than $632 \mu\text{m}$, the value of D^2/λ for the largest particles anticipated (20μ).

(6) The sixth condition calls for non-absorbing particles. It is true that this is not the case with Al_2O_3 , but it is also true that its absorption coefficient is 10^3 times smaller than the scattering coefficient for

the considered light wavelength, refractive index, and size numbers α . A very detailed discussion on the subject is presented by Plass [Refs. 36 through 38] where the absorption cross section $(\frac{n_2}{\rho})$ and the scattering cross section $(\frac{n_1}{\rho})$ are tabulated for different values of n_1 , n_2 and α ; n_1 being the real part of the refractive index, n_2 the imaginary part and $\rho = 2\alpha(n_1 - 1)$, the phase-shift factor. In the same work it is shown that the scattering cross section is about 2 times the actual cross section of the particle, while the absorbing cross section does not exceed 1.1×10^{-3} times the particle cross section (for $1.5 < n_1 < 2$ and $n_2 = 10^{-6}$, which is the case for Al_2O_3). Therefore, it can be assumed for the purposes of this experiment that the quantity of scattered light is about 2000 times larger than the quantity absorbed. This means that the latter will not substantially affect the results of the measurements.

The subject is discussed also by Wong, et al [Ref. 40], while Asano [Ref. 39] proved that "absorption causes a reduction of scattered intensity over almost the entire range of angles, except the forward scattering peak..." Figure 16 of that work shows the scattered light intensity for absorbing (refractive index $m = 1.5 + 0.1i$) prolate spheroids as approximately 10 times larger than for non-absorbing ones ($m = 1.5 + 0.0i$) for forward scattering angles between 0 and 15 degrees. The intensity of

scattered light remains larger than the absorbed one up to $\theta = 30^\circ$, which is well beyond the working angles for the present work.

Following the above discussion one would expect that the technique should work for absorbing Al_2O_3 as well. Incidentally, the absorption coefficient of Al and Al_2O_3 was not available for the wavelength of the He-Ne laser. The absorption coefficient of total radiation is given as 0.06 to 0.07 for rough-surface Al at 50 to 500°C and 0.2 to 0.3 for Al_2O_3 for the same temperature range [Ref. 42].

One further requirement, calling for an optical depth of $\tau_l < 1.5$, can be taken care of by properly regulating the density of the rocket exhaust particles or, more precisely, by properly choosing the distance of the laser beam from the exhaust nozzle.

An excellent discussion of the applicability and constraints of the forward light scattering technique is presented by Holve and Self [Ref. 43] in the context of introducing a related technique for "optical particle sizing for in situ measurements". Although that technique is quite different from the one used in this work, the theoretical considerations were practically the same for both. Thus, the two main factors involved in the practical realization of both techniques are (a) the control of the size and shape of the effective measurement volume and

the uniformity of response for different particle trajectories through it; and (b) the attainment of a response that is, as near as possible, monotonic with particle size and has minimal sensitivity to particle refractive index. These two factors are coupled in such a way that the optimum trade off is a function of the size range and concentration to be measured.

These two factors will be discussed later in this work, along with the experimental procedure.

B. OPTICAL ARRANGEMENT

A schematic diagram of the final optical set up is shown in Figure 10 and pictures of it are shown in Figure 11. The instruments and optical equipment used are listed in Table III. The optical equipment was mounted on an optical bench with one degree of freedom (vertical). A helium-neon laser was used as ~~the~~ light source. A spatial filter/beam expander located directly in front of the light source produced a uniform light beam with a one centimeter diameter. A plano-convex lens (5 cm in diameter with a focal length of 500 mm) was used as the condensing lens to focus the unscattered light beam on the aperture of the photosensor. The photosensor assembly had two degrees of freedom (vertical and horizontal) and consisted of a photodiode with a 5.1 mm^2 active area, its operating circuit, a narrow pass filter, and a small aperture (pinhole). The total length of the detector housing tube was 10 inches and its

diameter was 3 inches. The aperture plate was located 9 inches in front of the photodiode, so that the density of the light reaching the sensor would be well below the maximum allowed. The calculations involved with the required pinhole diameter and the pinhole-to-sensor distance are presented below.

The laser beam diameter coming out of the beam expander measured 11 mm. Without diffractively scattered light present the beam was coherent and parallel, so that its diameter was the same at the condensing lens.

The radius of the beam at the lens focal point is given by the formula [Ref. 41].

$$W_0 \approx \frac{\lambda f}{\pi W} = \frac{\lambda f}{\pi r_{\text{beam}}} \quad (7)$$

where $\lambda = 0.632 \mu\text{m}$, the wavelength of the He-Ne laser

$f = 500 \text{ mm}$, the lens focal length

and $W = r_{\text{beam}} = 5.5 \text{ mm}$, the radius of the beam coming out of the spatial filter/collimator

$$\text{Then } W_0 = \frac{6328 \times 10^{-10} \times .500}{\pi \times 5.5 \times 10^{-3}} = 0.018 \text{ mm}$$

A pinhole to let 99% of the light of an ideal beam to pass should have a diameter of [Ref. 41].

$$d_p = 6 \times W_0 = 0.108 \text{ mm}$$

A 0.153 mm pinhole was used for the calibration runs. For the actual runs, a 0.560 mm pinhole was employed because

(for reasons to be explained later) the beam radius was reduced to 1.09 mm. Then, the radius W_0 was 0.092 mm and the necessary pinhole diameter became 0.554 mm.

After passing through the pinhole the light was intercepted by the photodiode at the end of the housing tube. The latter was made long enough to ensure a spot on the sensor large enough so that the light intensity would be kept below the photodiode limits. On the other hand, the spot had to be appreciably smaller than the photosensor diameter so that the total amount of light would strike the sensor at its central area, and not at the periphery. In this way, any possible minor misalignment of the sensor with respect to the optical axis was taken care of and the spot was on the sensor under all circumstances.

C. EXPERIMENTAL PROCEDURE

An attempt to develop a "well behaved" apparatus set-up in an open test-cell of the Combustion Laboratory only proved the sensitivity of the technique to external noise sources (atmospheric particles, etc.). Therefore, the whole set-up was established inside a room and every precaution was taken to insure the absence of noise sources, such as dust, temperature changes and air movement.

After a collimated and filtered beam was acquired, the stability of the readings was checked using a digital voltmeter. Output voltage was found to be stable within 0.2 mV. The sensor tube was then translated throughout the

allowable span on both sides of the optical centerline. The forward scattered light (from air particles, optical components, etc.) was measured as a function of angle (translation) with no test particles present. Great care was taken during each run to avoid exposure of the photodiode to direct laser illumination. If this occurred accidentally for less than one second, enough time was allowed for the photodiode to recover. Longer exposure to intensities exceeding the maximum allowable for the photodiode permanently damages the exposed region of the detector.

Next, the accuracy of the Diffractively Scattered Light Method (DSL_M) for obtaining the mean diameter of particles was investigated. A comparison was made between experimentally obtained non-dimensionalized intensity ($I(\theta)$) versus non-dimensional angle ($\bar{\theta}$) profiles and the "universal" theoretical profile presented in Figure 9. Various profiles were obtained using glass beads of different sizes. Translation of the detector was done manually by means of a micrometer. The glass beads were suspended in distilled water contained in a home-made, plexiglas 2.5" x 3.0" x 2.5" container. A magnetic stirrer was used to assure a constant density of glass beads in suspension. The same stirrer was used for the light-scattering measurements of plain water for the same reasons, since the water could not be taken as without any foreign particles in it.

Thus, the intensity profiles for plain water, as well as for 53-64 μm , 37-44 μm and 1-37 μm glass beads were determined. The measurements would start at a relatively large (for the given size of particles) distance from the centerline and continue until an abrupt increase of the output voltage would be noticed. An abrupt increase would not result from the intensity of forward scattered light, but rather from transmitted light. The DSL intensity at the centerline was found by extrapolating the "near-centerline" profile. Experience showed that the last reliable measured voltage would be at a distance from the centerline of 2.5 to 3 times the pinhole diameter. The measured voltages in each case were plotted against the distance from the centerline as shown in Figure 12. Then $I(\theta)$ versus $\bar{\theta}$ curves were constructed for each case by calculating the pairs of values from the definitions:

$$I(\theta) = \frac{I_{\theta,p} - I_{\theta,o}}{I_{cl,p} - I_{cl,o}} = \frac{V_{\theta,p} - V_{\theta,o}}{V_{cl,p} - V_{cl,o}} \quad (8)$$

where , I_{cl} or V_{cl} are the extrapolated light intensity and related voltage at the centerline, and I_o and V_o are the light intensity and voltage at an angle θ . (Figure 13). o and p symbolize "no particles" and "with particles", respectively.

Also
$$\bar{\theta} = \frac{\pi D_{32}}{\lambda} \theta \quad (9)$$

In Equation (16) D_{32} for the spherical particles was taken to be the mean diameter. The latter was determined from SEM photomicrographs. $I(\theta)$ versus $\bar{\theta}$ curves are plotted for each bead sample and compared to the theoretical profile in Fig. 9. It was found that

- (1) large deviations from the universal curve occurred at $\bar{\theta}$ larger than 3 to 4 and
- (2) the agreement with the universal curve was dependent on the sample mean diameter with deviations increasing as \bar{D} decreased.

Both of these limitations could be related to the far from ideal conditions in the test area, namely; to the influence of the plexiglas walls of the container on the scattered light and the multiple reflections on the walls. Obviously the ratio of the non-diffractively scattered light (noise) over the diffracted one was increasing with increasing θ , due to the aforementioned reasons.

The much larger discrepancy for the 1-37 μm sample was also largely related to the fact that the inaccuracy of the DSL technique increases as the ratio $\frac{\bar{D}}{D_{\infty}}$ decreases, where D_{∞} is the largest diameter expected in the sample [Ref. 23].

By the same procedure (Figure 14) the $I(\theta)$ versus θ curve for a sample of Al_2O_3 powder with mean diameter 91 μm was constructed (Figure 9). Two different aluminum oxide particle number densities were used with transmittances

of $\frac{E}{E_0} = 0.34$ and $\frac{E}{E_0} = 0.17$. The second transmittance was obviously below the suggested limit of 0.223 (Equation 10), but it was chosen for comparison purposes. The profiles obtained are shown in Figure 9. A very close agreement with the universal profile was noticed at $\bar{\theta} < 2$. It should be noted that for this sample the maximum diameter present was $D_\infty = 140 \mu\text{m}$. Thus, $\frac{\bar{D}}{D_\infty} = 0.65$ and this can account for the deviation from the universal curve along with the non-spherical (non-ideal) shape of the aluminum oxide particles.

Three basic conclusions were drawn from the above calibration experiments:

1. The diffractively scattered light technique works reasonably well using a photodiode instead of a photomultiplier tube as used by previous investigators [Refs. 16, 25, etc.].
2. The accuracy of the data obtained was very good at small $\bar{\theta}$ and high $\frac{\bar{D}}{D_\infty}$. As mentioned earlier, small $\bar{\theta}$ were necessary to neutralize the effects of the container walls. The problem was compounded for particles with smaller mean diameters, since accurate measurements are required at larger scattering angles.
3. The deviation from the universal curve increased with decreasing $\frac{\bar{D}}{D_\infty}$. This was especially noticeable in the 1-37 μm sample curve where $\frac{\bar{D}}{D_\infty} = \frac{14}{37} = 0.378$ and the spectrum of the diameter sizes was broader. This is very

well explained from examining Equation (9), describing the integrated light scattering profile. The equation indicates that the relative contribution due to the various particle sizes is proportional to D^4 , so that the influence of the smaller particles in the polydispersion is negligible. [Ref. 23].

Next the DLS measuring set-up was transferred to the test cell where solid propellant motor firings were to be performed. A wooden box (with the necessary access doors) covering the whole experimental set-up was constructed to protect the optics and to minimize the effects of external contaminants (dust, light, etc.).

Several runs were then made to establish the sensitivity of the measurements to the measurement volume and the particle concentration. It was noticed that there was a limit to the effective measurement volume, defined by the laser beam and the edges of the exhaust cone. First of all, the beam diameter had to be smaller than the height of the exhaust cone at their intersection so that the light would scatter on a volume with a "uniform-density" of particles. The beam diameter had to be further reduced so that interference would be avoided. The latter will occur when the scattered light from one particle is significantly enhanced by scattered light from other particles present in the measurement volume within the resolving time of the electronics [Ref. 23]. The result of this phenomenon was

an "averaging" effect, leveling off the forward scattering intensities at different angles θ .

The interference problem was quite probably enhanced by other effects, like the beam deflection due to the temperature gradients (ambient temperature air - exhaust stream - ambient temperature air), as well as due to the edges of the conical exhaust stream.

Any possible influence of the exhaust shocks on the beam characteristics was avoided by positioning the beam centerline at a downstream distance larger than 10 times the nozzle diameter.

A black home-made screen with a hole at the center was successfully used to reduce the beam diameter reaching the particles to 2.2 mm, so that the effective measurement volume could be reduced and the problems mentioned above eliminated.

For the actual runs, a cylindrical motor (Figure 11) made out of stainless steel was used with a copper nozzle that had a 0.110 inches throat diameter. A cylindrical piece (1.2" diameter, 1.0" long) of NWC-1 propellant was burned (1.0% by weight of 8 μ m diameter) Al_2O_3 . The whole set-up is shown in Figure 15 and a schematic of it in Figure 10. The combustion pressure was recorded on a Visicorder oscillograph along with the photodiode output voltage. The latter was also recorded on an oscilloscope with provision for taking pictures of the trace. A home-made translation mechanism was used for the

photosensor to scan the intensity profile of the scattered light. A linear potentiometer was also employed to determine the distance traveled by the sensor. Table III lists the experimental apparatus used.

The translation mechanism had a travel distance of 1.938 inches and was energized remotely by means of an electric solenoid. The motor firing was also done remotely. An aluminum tube surrounding the exhaust jet was used to restrict the exhaust particles, protect the optics, and also to allow collection of particles for microscopic examination.

The actual runs of the DSL experiments started with calibration of the recording equipment. The focal point of the laser beam after the condensing lens was placed at a distance of 3 mm from the pinhole centerline. This offset distance was chosen as a compromise between the Visicorder input voltage limits and the necessity for the recording of low voltage values corresponding to intensities far from the pinhole, (i.e., for getting a reasonable sensitivity).

When the electric solenoid was energized the pinhole and the sensor scanned the scattered light intensity for a horizontal distance of 1.938 inches.

A "cold" run was done first, with no particles in the scene volume and the "zero scattering" profile was recorded. Then the motor was fired.

When the pressure in the combustion chamber reached a constant value (190 psi), the solenoid was activated. The constant-pressure burning lasted for 7 seconds and the scanning commenced at about 2 seconds after constant pressure was reached. The DSL intensity was again recorded versus time and traveling distance of the pinhole. The profiles from the two runs are presented in Figure 15, traced from the Visicorder paper.

Using Figure 15 the scattered intensity (voltage) at the centerline was found by extrapolation for the "cold" run (163.9 mV) and the "hot" run (183.1). Then several distances from the pinhole were picked and $I(\theta)$ was calculated for each one as described earlier. By using the "universal curve" (Figure 9) the corresponding values of $\bar{\theta}$ were obtained. The volume-surface mean diameter D_{32} was calculated from the equation $\bar{\theta} = \pi D_{32}^3 / \lambda$. The values obtained are tabulated in Table IV.

The mean diameter D_{32} was also calculated using the calibration curve obtained for glass beads of sizes 1 to 37 μm (Figure 9), since the mean diameter of the exhaust particles falls within this interval. The results are also tabulated in Table IV.

Residue of the exhaust particles was collected from the aluminum tube. Some of it was cleaned by means of acetone and an ultrasonic vibrator, and then dried in a vacuum oven. Both "clean" and "as-collected" samples of

the residue were examined with an SEM. Pictures are shown in Figures 16 and 17, respectively. From these pictures the diameters of the Al_2O_3 and other particles were measured. Their distributions are shown in Figures 18 and 19 for "clean" and "as-collected" samples, respectively. The mean diameter for each was then calculated.

Comparing Figures 16 and 17 one can see that in the latter only a relatively few Al_2O_3 particles (of circular cross-section) are present. The other residue appears to be from the inhibitor used on the sides of the end burning grain. The Al_2O_3 particles had a mean diameter of $7.4 \mu\text{m}$, e.g., practically the same as the original particles cast in the propellant (Figure 16). The presence of large amounts of inhibitor residue obviously affected the scattered-light intensity profile and the calculations. Therefore, the quantity of inhibitor used in future experiments should be minimized.

D. DISCUSSION OF RESULTS

The volume-surface mean diameter D_{32} of the exhaust particles is tabulated in Table IV as a function of the forward scattering angle θ . A large deviation is observed at $\theta = 0.012$ rad, which probably was related to the inaccurate determination of the output voltage at that angle due to the voltage - curve being very steep in that region (Figure 15). Therefore, this value of D_{32} should be disregarded.

The remaining larger angles resulted in an average D_{32} of approximately 20 μm with a spread of approximately 1.3 μm , when the "universal curve" was used. Reference 25 suggests that the best choice for determining D_{32} is the region near $I(\theta) = 0.08$, where the standard deviation as calculated from different distributions of droplet size is only slightly greater than 1%. Following this advice $D_{32} = 19.4 \mu\text{m}$. This value was 1.69 times larger than the measured (SEM) mean diameter of the exhaust particles. A small part of this difference may be related to the fact that D_{32} is about 10% greater than the mean diameter, when the particles are not all the same size spheres. In addition, the ratio of the irregularly shaped exhaust particle surface area to their mean diameter is expected to be larger than for a sphere for which the theory is developed.

However, if the calibration curve for particles of diameters 1-37 μm (Figure 9) was used instead of the "universal curve", the average D_{32} was found to be approximately 11.8 μm (approximately 11.2 μm with $I(\theta) \cong 0.08$). Both values were in good agreement with calculated mean - diameter of 11.5 μm .

As discussed earlier, the deviation from the "universal curve" increases with decreasing $\frac{\bar{D}}{D_{\infty}}$ (in the present case $\frac{\bar{D}}{D_{\infty}} \cong \frac{11.5}{115} = 0.1$). Equation (2) indicates that the relative contribution due to the various particle sizes is

proportional to D^4 , so that the influence of smaller particles in the polydispersion is negligible [Ref. 23]. This can quite possibly explain the "failure" of the "universal curve" to predict the right size of D_{32} for the present experiment, and the volume-surface diameter being estimated considerably larger than the mean diameter of the exhaust particles. On the other hand, the calibration curve for 1-37 μm particle size has already incorporated the influence of the small $\frac{\bar{D}}{D_\infty}$ and therefore was more appropriate for use in the experiment.

It is suggested that more runs be made with the developed set-up for the above conclusion to be verified. If the conclusion can be validated, the DSL method should be used with D_{32} estimated from $I(\theta)$ versus θ calibration curves appropriate for the expected size intervals.

It is also suggested that the time of traverse of the photodiode detector be increased so that more accurate data can be extracted from the illumination profiles.

TABLE III
EXPERIMENTAL APPARATUS
FOR DSL METHOD

1. Spectra Physics Model 147, Helium-Neon Laser.
Power 5 mW, Random Polarization.
2. Power Supply for above, Model 247, 30 watts.
3. Voltage Regulator.
4. Laser Beam Expander with spatial filtering,
22 mm aperture, Oriel, Model 1526.
5. Plano-convex collimating lens, 5 cm diameter.
50 cm focal length.
6. Photodiode, EG & G type UV-215B.
7. DC power supply for the photodiode circuit.
8. Hewlett-Packard, AN/USM=310(V)2 Oscilloscope.
9. Honeywell, Visicorder Oscillograph, Model 2106.
10. Teledyne, Pressure Transducer, Model 206-SA.
11. DORIC, Integrating Microvoltmeter, Model DA-100.

TABLE IV

VOLUME-SURFACE MEAN DIAMETER (D_{32}) MEASUREMENT RESULTS

DISTANCE FROM OPTICAL C.L. (IN)		FWD ANGLE	OUTPUT VOLTAGE (mV)		$I(\theta)$	$\bar{\theta}$		D_{32}
ON CHART	TRUE	θ (rad)	COLD	HOT		Universal Curve	1-37 μ Cal.	
0	0	0	163.9	183.1	1.00	0	0	-
.430	.231	.012	132.8	138.6	.30	1.82	1.08	18.1
.700	.377	.019	36.5	40.3	.20	2.08	1.25	13.3
.840	.452	.023	17.3	20.3	.16	2.25	1.35	11.8
1.010	.544	.028	7.7	9.0	.07	2.83	1.63	11.7
1.150	.619	.031	3.5	4.8	.07	2.83	1.63	10.5
$D_{32} = \frac{\lambda \bar{\theta}}{\pi \theta} = .201 \frac{\bar{\theta}}{\theta}$								

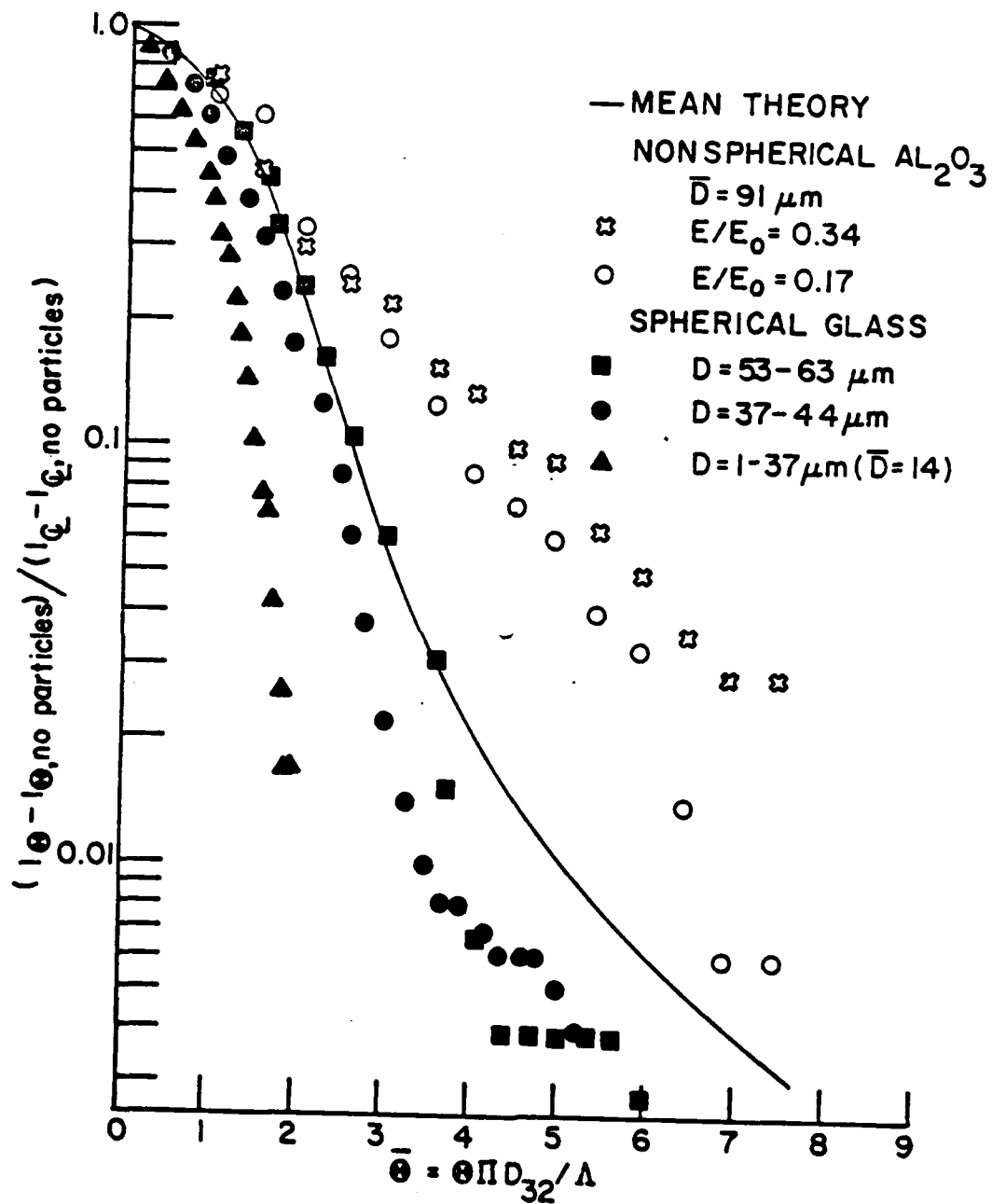


Fig. 9. Nondimensionalized Illumination Profiles
[$I(\theta)$ versus $\bar{\theta}$]

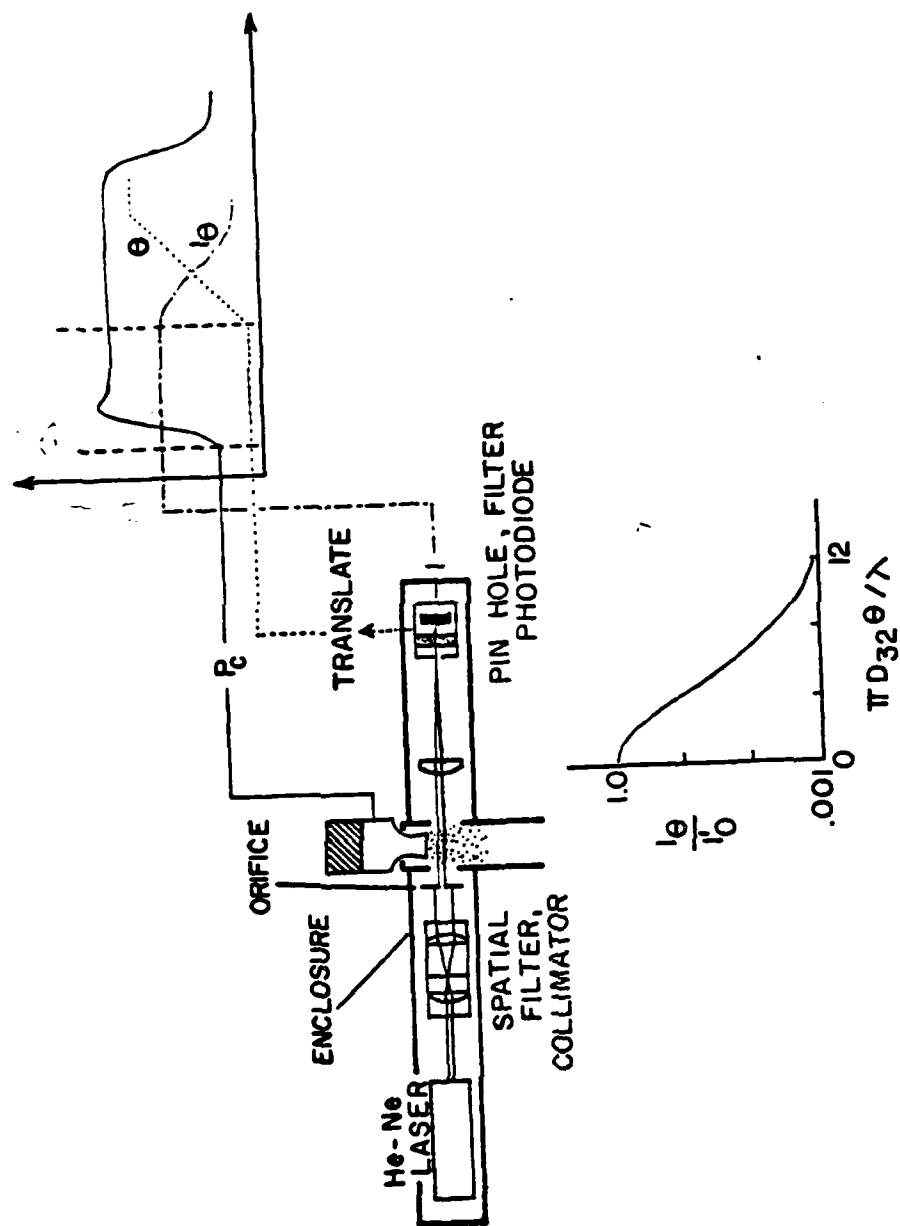


Fig. 10. Schematic Diagram of Diffractively Scattered Light Apparatus

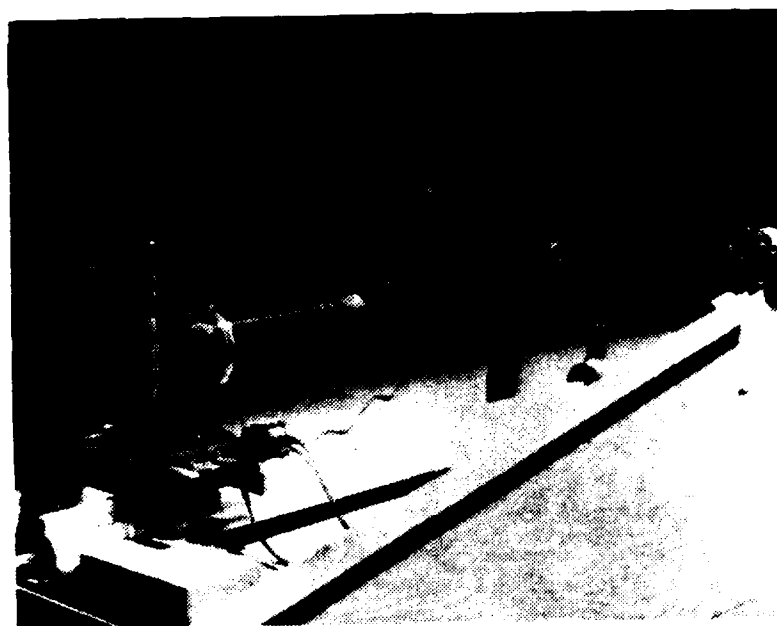


Fig. 11. Photographs of Light Scattering Set-up

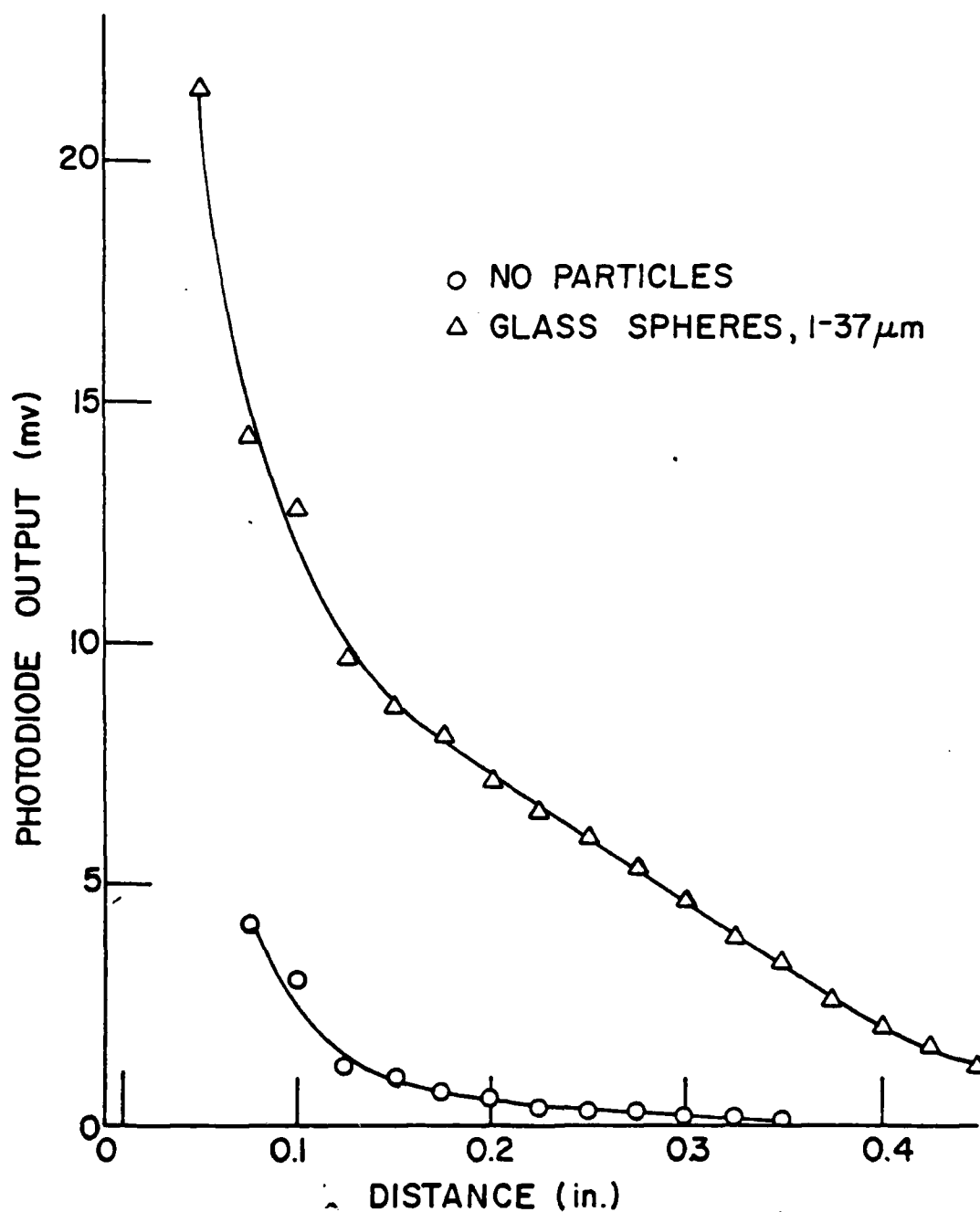
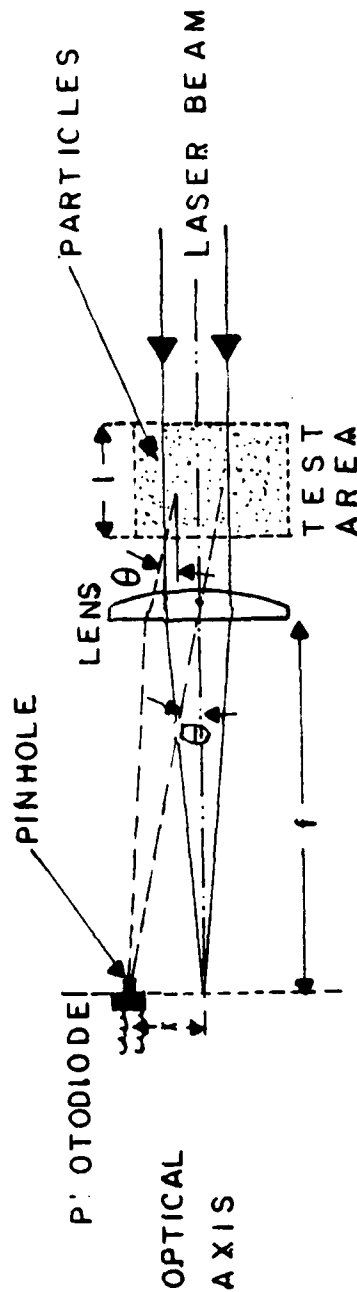


Fig. 12. Photodiode Output Voltage versus Distance from Centerline for Glass Beads



For air: $\theta \cong \frac{x}{f}$

For water: $\theta \cong \frac{x}{f \times 1.35}$, where 1.35 is the refractive index of water [Ref. 21]

Fig. 13. Light Scattering Geometry

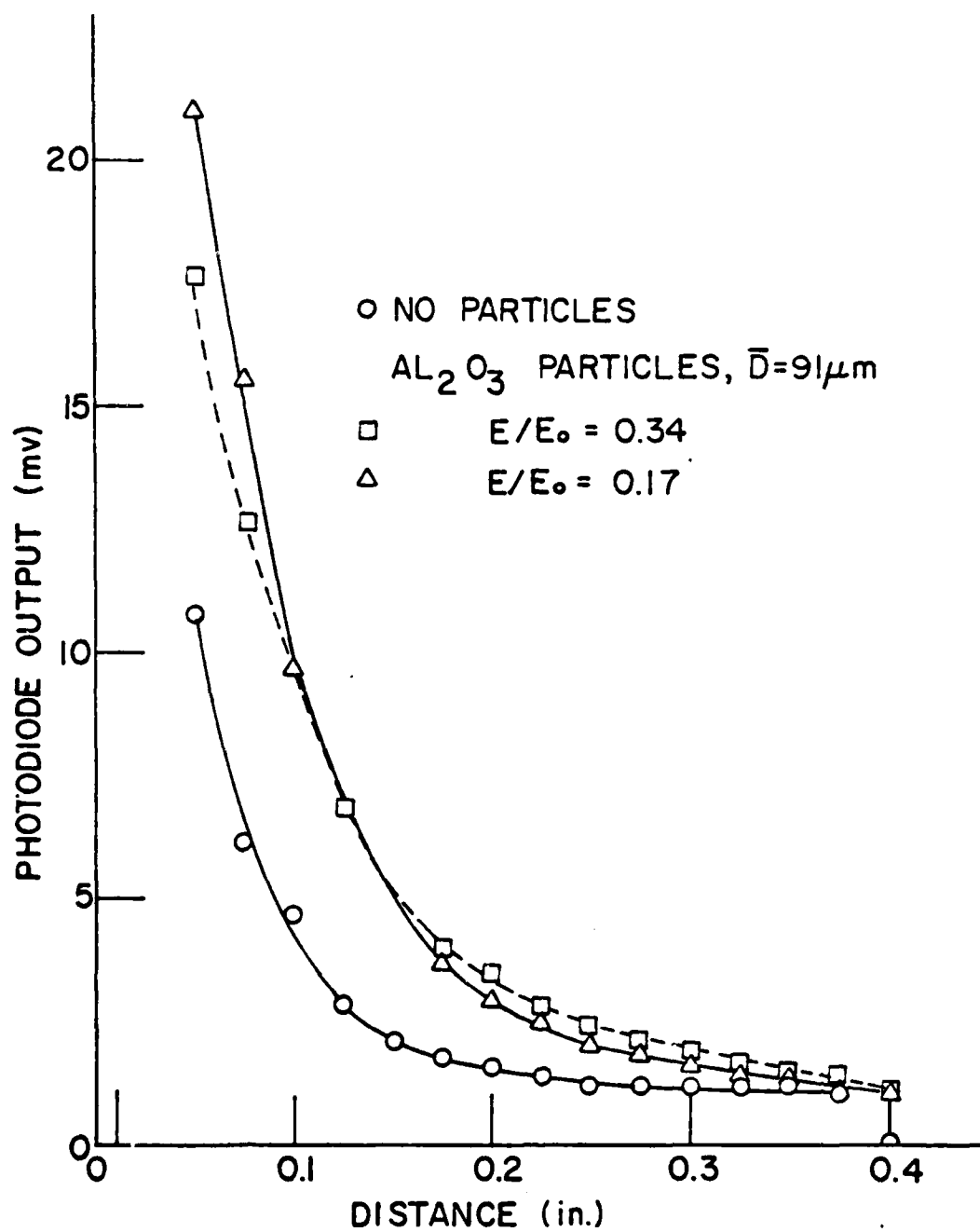


Fig. 14. Photodiode Output Voltage versus Distance from Centerline for Al_2O_3 Particles

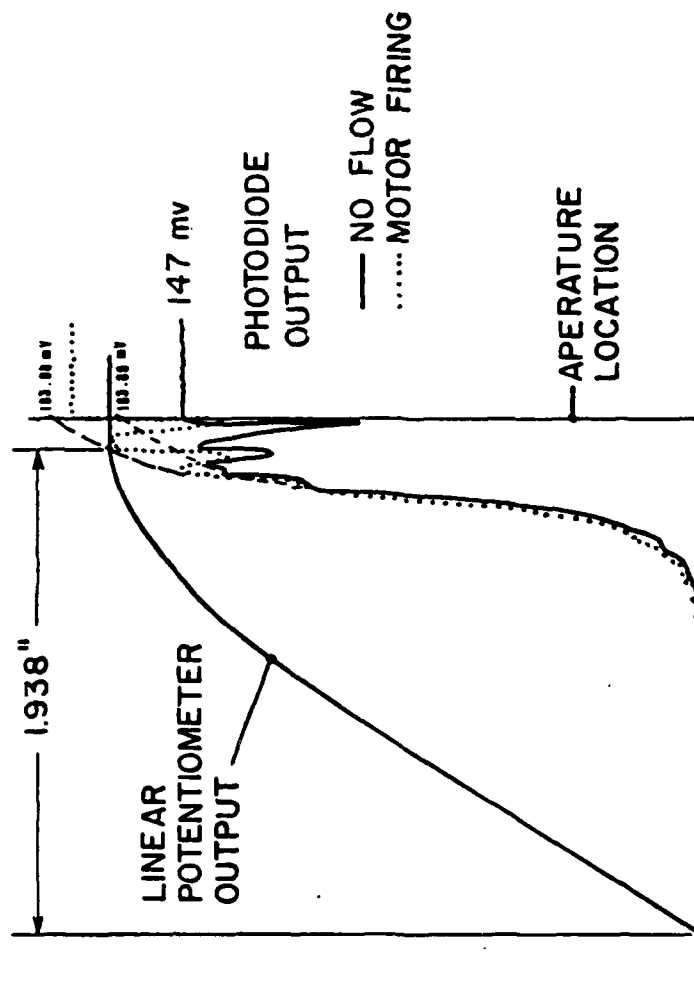


Fig. 15. Photodiode Output-Voltage Profiles versus Distance from Optical Centerline (actual runs)

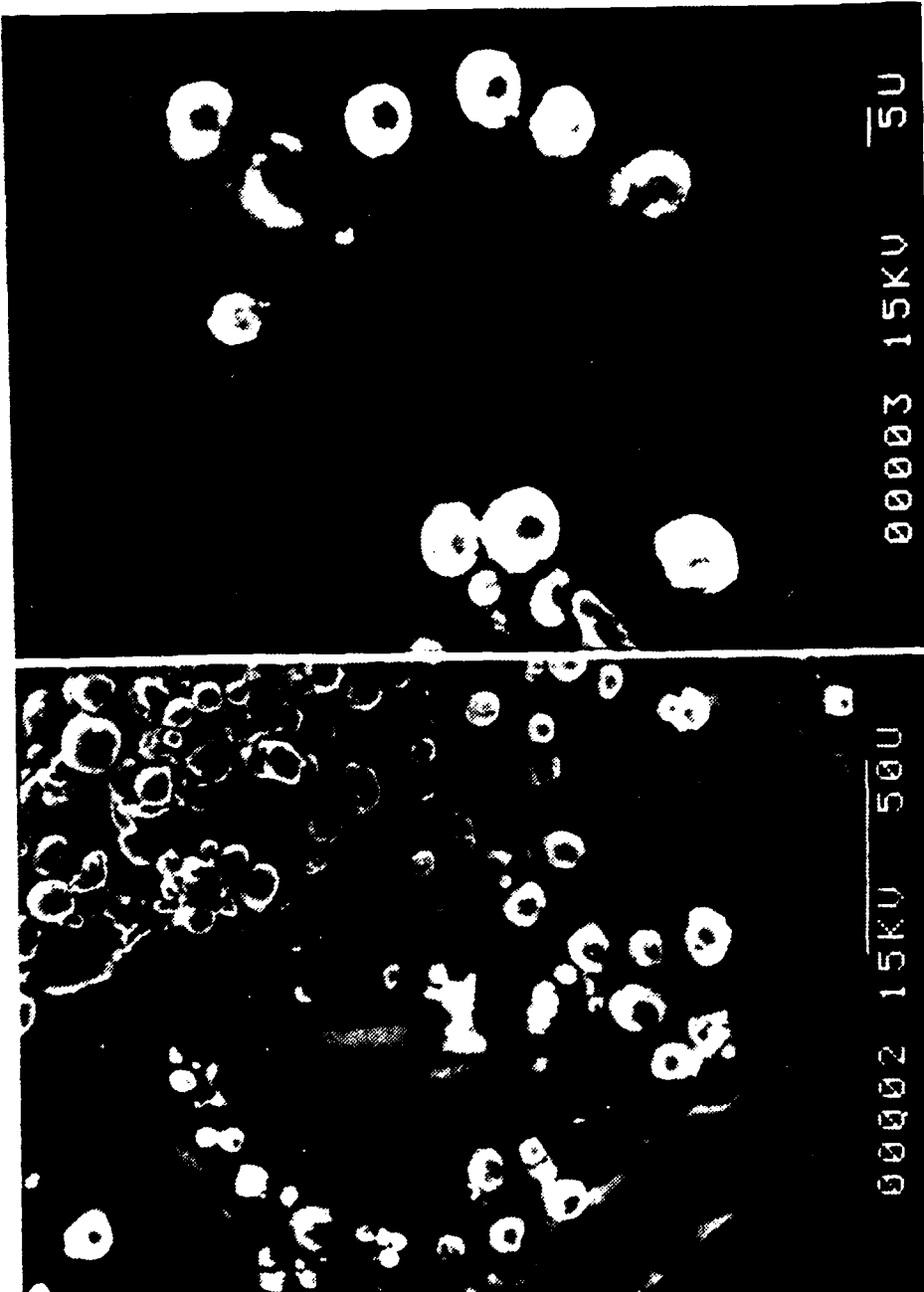


Fig. 16. SEM Photomicrographs of Rocket Exhaust
Particles (clean)

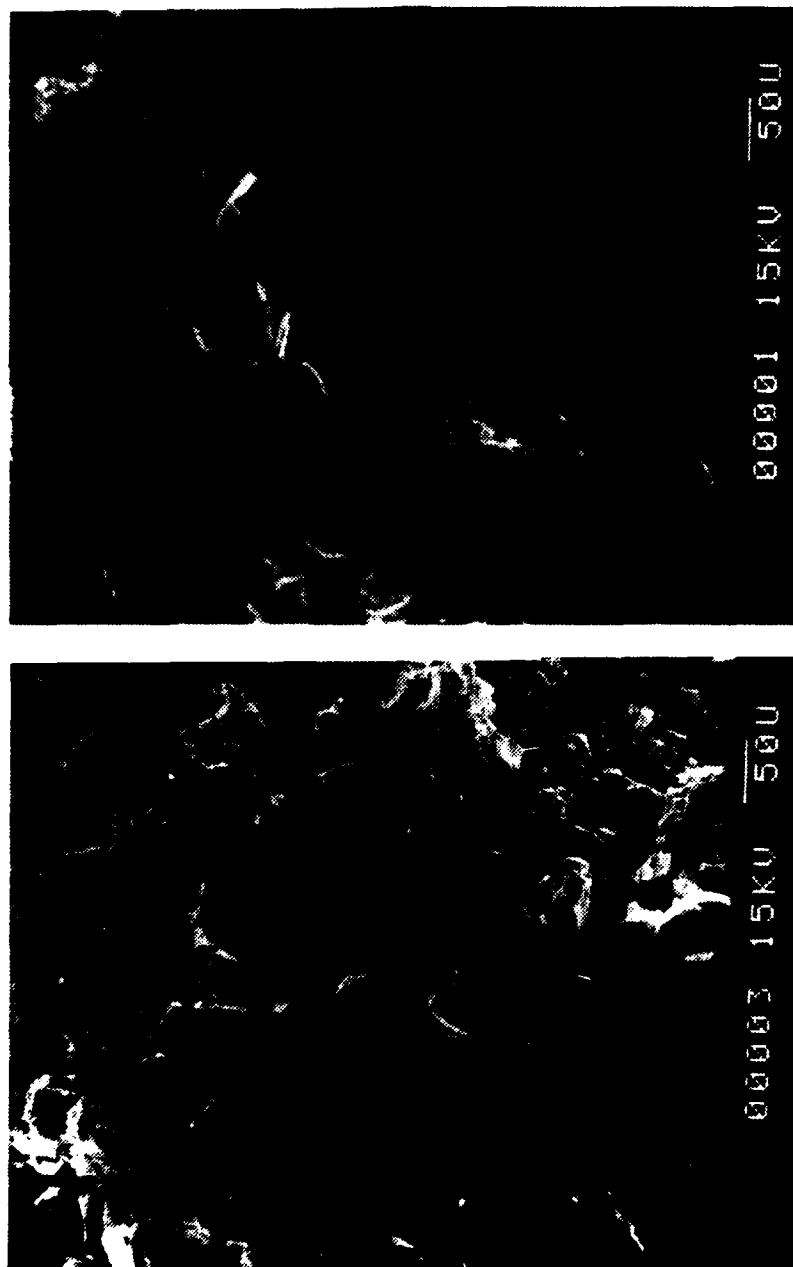


Fig. 17. SEM Photomicrographs of Rocket Exhaust
Particles (as-collected)

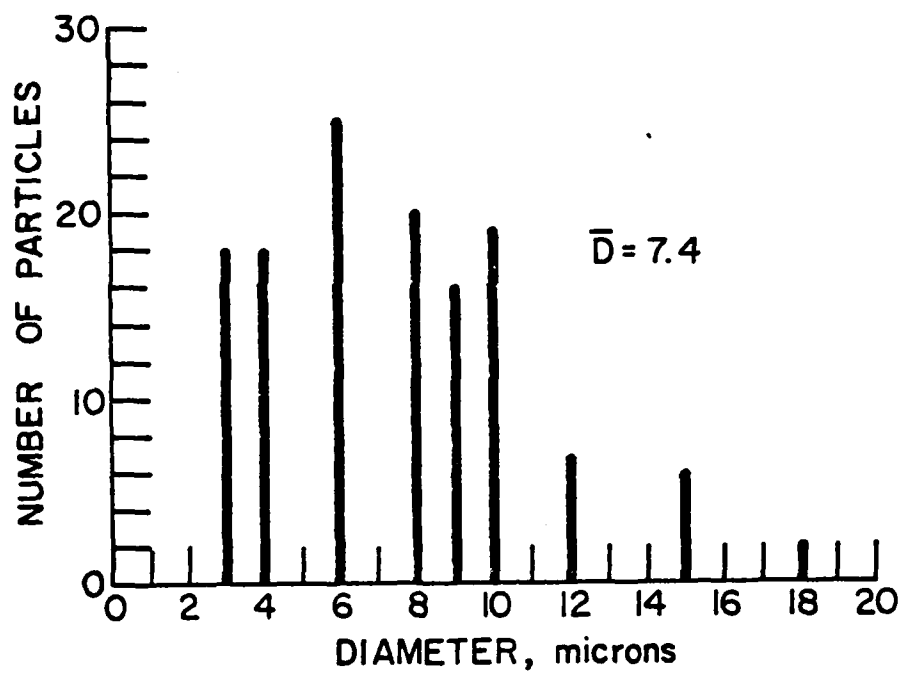


Fig. 18. Size Distribution of Clean Exhaust Particles from Propellant NWC-1, Burned at 190 psi

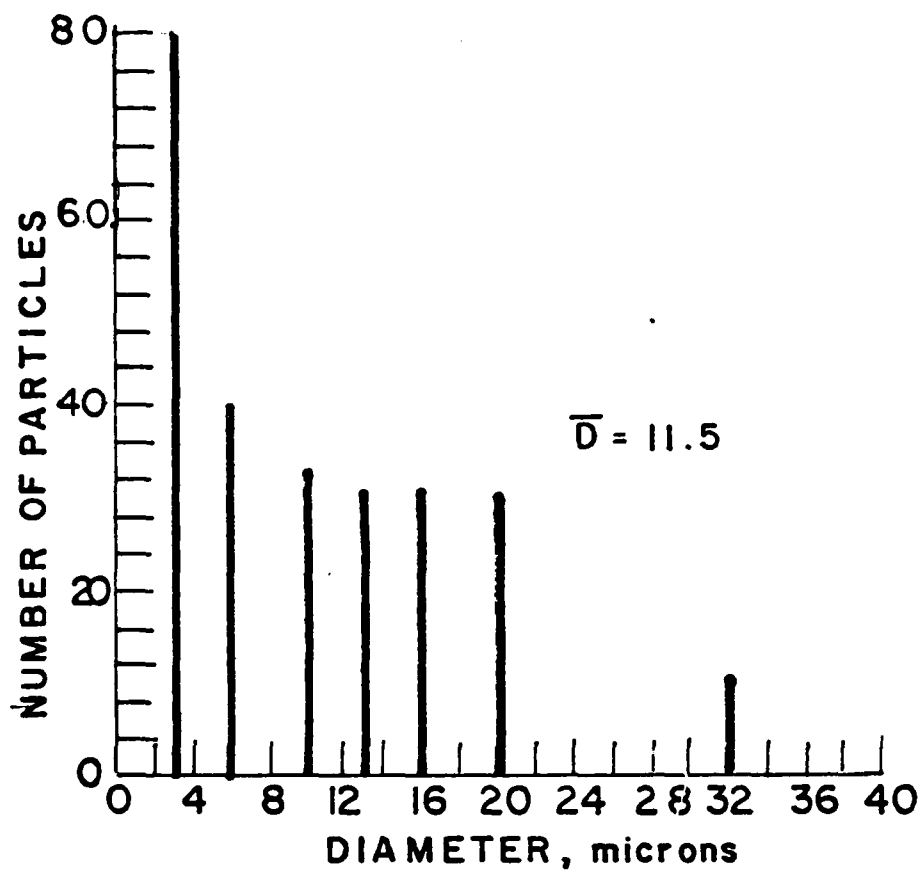


Fig. 19. Size Distribution of (As-Collected Exhaust Particles) from Propellant NWC-1, Burned at 190 psi

V. HOLOGRAPHIC METHOD

A. INTRODUCTION

Holography is a technique used for recording of visual information. It is different than classic photography in that both amplitude and phase information are recorded. By means of proper illumination of the developed record by this technique (hologram), a three-dimensional image of the original scene can be obtained. A thorough theoretical base exists and can be found in references such as [44] and [48]. Holographic systems have been used since the mid-sixties for recording relatively large volumes of particles in the size range from 3-1000 μm mean diameter [Ref. 47]. The technique has been applied to solid propellant combustion diagnostics through particle size analysis [Refs. 45 & 46]. Such a hologram is a composite interference pattern of the far field diffraction pattern of the particles and the undiffracted background illumination. The use of a pulsed laser as the holographic light source satisfies the requirements for a high degree of spatial and temporal coherence while limiting the exposure time. In this manner, rapidly changing events can be recorded without significant image blurring (within limits, of course). The high light intensity of the laser, on the other hand, makes possible the use of very fine grained film with slow emulsions. Such emulsions provide a very high image resolution. The nature

of the laser light also makes possible the recording of combustion particles despite the presence of a considerable amount of flame and smoke. These holograms are called Fraunhofer or far field holograms due to the fact that the hologram is recorded at a distance that is effectively in the far field of the object. For blurring of the recorded particles to be avoided, the particle should not move more than one tenth of their mean diameter during the exposure. The experimentally determined sample depth for recording and reconstructing aerosol particles of mean diameter d is $49(d^2/\lambda)$ where λ the wavelength of the illumination [Ref. 47]. This depth is over three orders of magnitude more than if conventional high resolution photography were used. Another advantage of the holographic technique over the latter (very significant for particle size measurements) is that, when a plane wave is used for the recording and construction, the magnification is uniform over the entire recorded volume. If plane waves of different wavelengths and λ_2 are used for recording and reconstruction (as the case in the present experimentation), the location of the reconstructed real image is related to the location of the original object by the factor λ_1/λ_2 , i.e.,

$$z_2 = (\lambda_1/\lambda_2)z_1$$

Therefore, the reconstruction plane is moved but magnification remains unity and is independent of the distance from the recording plane to the object.

Unwanted features of the holographic technique include noise originating from the film granularity and optical imperfections as well as aberrations. Aberrations other than those inherent in the hologram process can arrive from the recording camera lenses and the rest of the optical pieces used. Nevertheless, aberrations introduced during the recording can be minimized during the reconstruction process by employing the same camera lens, etc., and hence introducing compensating aberration terms [Ref. 47].

B. EXPERIMENTAL APPARATUS

A lens-assisted-holographic system was used as described in Refs. 45, 49 & 53 and shown schematically in Figures 20 and 21. Its main difference from the conventional holographic arrangements is the rigid attachment of a pair of focusing plano convex lenses to a kinematic plate holder. This pair operated at 1 to 1 with an input numerical aperture of 0.24 (5-cm diameter, 10-cm working distance) and had the purpose of forming images of the subjects in the vicinity of the holographic film.

The comparatively large numerical aperture provided for the needed resolution. It is not desirable to form a sharp image at the recording plate plane as saturation effects would limit the faithfulness of the reconstruction. Hence, a lens is used in which the aberrations are not fully corrected. The hologram now records only over a small area

of the phase and amplitude of the aberrated wave front incident upon it.

High resolution is achieved in reconstruction by playing the image back through the same lens used in recording, since, by so doing, aberrations due to lenses are holographically eliminated [Refs. 47 & 53]. This is the reason why the focusing lenses were rigidly attached to the kinematic plate holder. The method of reconstruction is shown schematically in Figure 22. As illustrated, the three-dimensional recreated images were examined with a conventional microscope using various objective lenses and eyepieces.

For recording holograms the "rebuilt" AFRPL ruby laser illuminator described in Ref. 54 was used. The system consisted of a double Kerr cell Q-switched oscillator, a pulse chopper, a ruby laser amplifier, and an electro-optical half-wave plate (Kerr cell). When operated in the Q-switch mode, the system emits single or double Q-switched pulses of approximately 1 Joule total energy and approximately 50 nanosecond duration at 0.6943 microns. A Kerr cell is used on the output of the amplifier for controlling the polarization direction of the double pulses, when needed. The pulse chopper reduces the duration of a single pulse to < 10 nanoseconds. Similarly, the pulse energy is reduced to a maximum of approximately 0.25 Joule. Pictures of the different components of the ruby laser illuminator system are shown in Figure 23.

For the image reconstruction, a Spectra-Physics Model 125, He-Ne gas laser was employed with a nominal power output of 50 milliwatts (CW uniphase at 0.6328 microns). Its 1/e diameter was approximately 2 mm (Figure 24).

AGFA-GEVAERT 8E75 HD plates were used for recording the holograms.

Opposed slabs of propellant could be burned in a two-dimensional motor (Figures 25 and 26) with an internal volume of about 1 cubic inch and designed to withstand pressures up to 3000 psi. The motor was designed with two 0.5 inch diameter, high-quality glass windows to allow for the recording of the burning. Nitrogen purge was provided from the bottom of the motor for keeping the windows clean by posing an obstacle to the combustion products. The latter system was found insufficient when "large" quantities of propellant (slab motors) were burned. The motor was therefore modified by adding a shutter in front of each window. The shutters (Figure 27) would remain shut, protecting the windows until the chamber pressure reached the desired value. At that time a pressure switch - time delay - solenoid - microswitch mechanism allowed the shutters to open and the laser to fire.

The propellant was introduced into the motor either as slabs bonded on opposing bases at right angles to the windowed walls, or as small strands attached to a pedestal (Figure 26).

The whole sequence was remotely controlled and monitored. A Honeywell Visicorder was also used for monitoring the combustion chamber pressure and the sequence of the events (pressure switch energizing, shutter opening, laser firing) so that proper adjustments could be made.

C. EXPERIMENTAL PROCEDURE

Practically all holograms were recorded by changing the collimated mode of scene illumination to a diffused one, by means of a ground glass diffuser. This had to be done since the collimated - mode scene beam caused sharp refractive effects. At higher pressures and with highly metallized propellants the refraction by the thermal cells prohibited identification of particles.

Various glass diffusers of different opacity were used for different types of propellants. The "optimum" (for each propellant - pressure combination) diffuser was determined experimentally. Essentially, as more smoke was produced, a more intense scene beam was required. This required a less opaque diffuser glass. Along with each diffuser a neutral density filter of "matching" transparency was used to reduce the light intensity of the reference beam and bring it to the correct intensity ratio with the scene beam.

Thermal cell effects were minimized with the diffuse light, since the illuminating light was scattered evenly over a wide range of angles and as a result, the thermal

cells were averaged [Ref. 53]. The presence of thermal cells was still observed with highly aluminized propellants but within tolerable limits, not affecting the particulate discrimination. Another problem, however, was introduced by the use of the diffusers. This was the reduced resolution due to speckle effects. These effects were further enhanced due to the fact that a CW He-Ne laser was used for the reconstruction.

For each run the holographic glass plate was installed into the kinematic plate holder under dark conditions and the holder was placed within the holocamera frame. After exposure the plate was removed and developed.

Developing was done as follows:

- (1) The plate was bathed in Kodak D-19 developer. The plate was periodically inspected during the development under a "Kodak OC filter safelight" in order to optimize the developing time (approximately 1-3 minutes). The time in the developer could not be fixed since the exposure of each plate was different due to the different recording conditions (amount of smoke, neutral density filter).

- (2) When the negative intensity appeared correct according to previous experience, the plate was rinsed momentarily in water and then placed in Kodak "Rapid Fix" for 5 to 7 minutes.

- (3) A water-wash followed for a minimum of 15 minutes.

(4) The plate was then placed in Kodak "Photo Flo" solution for 30 seconds.

(5) The plate was hung to air-dry for several hours.

The developed plate was then repositioned into the kinematic holder and the He-Ne laser was used for reconstruction.

In some of the reconstruction a revolving mylar disc was used at the reconstructed object location. This was done to suppress speckle during observation and picture taking [Ref. 53]. Kodak Plus X film was used for the pictures.

Strands of 5 different propellants were burned under pressures of 500 and 1000 psi. The propellants and some related data are listed in Table V. Prints from the resulting holograms are shown in Figures 28 through 37 together with corresponding pictures taken with the high-speed cinematography method. The latter were obtained from the films taken by Diloreto [Ref. 17].

D. RESULTS AND DISCUSSION

The resolution obtained in holograms without propellant burning was $11 \mu\text{m}$, as seen in a photograph of the 1951 USAF Resolution Target in Figure 28 ($5/4 = 11 \mu\text{m}$). It should be mentioned that resolution and clarity on the pictures presented in this report are not as good as seen with eye through the microscope. The camera used created focusing problem (with the specific application) due to the

ground glass incorporated as a focusing plate. The focusing problem became even worse when the speckle removal technique (mylar disc) was applied; an opaque object (the image on the mylar disc) was attempted to be focused on the opaque plate of the camera). Furthermore, in this initial effort the critical focus of the microscope on the mylar disc was not well controlled. For these reasons the pictures taken with the speckle removal technique are slightly out of focus.

A major problem in the recording of the strand burning was introduced by the smoke. The strand size had to be limited to a width of 4 mm and depth of 1 to 1.5 mm. In this way the quantity of the smoke was kept low enough for the scene beam to penetrate. The opacity of the gases in the scene required that the intensity of the reference beam be reduced by means of neutral-density filters. This was necessary to maintain the necessary intensity ratio of the two beams. The problem could quite possibly be alleviated if the laser power was higher.

The insufficiency of the available laser power was also apparent when propellants with very small aluminum particles were burned. Thermal cells were introduced in that case and the only way to eliminate them after the use of a diffuser in the scene beam (which further reduced the laser intensity) was to use a pulse with a shorter duration than 50 μ sec (i.e., 10 μ sec). This resulted in even less

available laser power and, therefore, most hologram were taken with a 50 μ sec pulse.

A possible remedy for the laser power problem would be to change the diverging lens in the Ruby laser, thereby reducing the beam size and consequently, increasing the power density of the beam. Only about one quarter of the present diameter is used for the scene beam. This reduction in beam size, however, may result in less coherence and resolution capability.

As mentioned earlier, a 0-80 screw was used on the side of each burning strand as a scale reference. The peak-to-peak distance between the screw threads was 317.5 μ m . When a 5X eyepiece and a 1X objective were used in the microscope for picture taking with the 35mm camera, the scale on the pictures was approximately 1443 μ m/inch. With a 5X eyepiece and a 2X objective the scale was approximately 1084 μ m/inch. Comparing these pictures with the ones obtained through high-speed cinematography [Ref. 17] it should be mentioned that the scale on the latter was approximately 2800 μ m/inch.

No agglomeration and no noticeable pressure effects on mean particle diameter were observed in the holograms. This agreed with the SEM data presented in Ref. 17.

Actual sizes of the particulates can be readily obtained from the holograms, eliminating the flame envelopes present

in the movie pictures. The particle sizes measured from the holograms were the same as those in the cast propellant, in agreement with the post-fire residue analysis reported in Ref. 17.

Each photograph of a hologram has very limited depth of field and therefore includes limited particles. The need is obvious for automatic data processing to obtain particle size distributions from the entire hologram. The pictures presented in this work were taken only to demonstrate what is contained in typical holograms.

Holograms were successfully obtained of a propellant with 15% aluminum by weight (propellant N-7, Figure 35). Thus, the technique can be used to study the combustion behavior of a wide range of propellants.

The speckle removal technique greatly improved the resolution when holograms were observed through the microscope. The camera focusing methods must be improved in order to record these better data.

VI. CONCLUSIONS AND RECOMMENDATIONS

The resolution and magnification capabilities of the high-speed cinematography system were improved to 14 μm and 1.12X, respectively. This was accomplished at the expense of the depth of field. Thus, as expected, a compromise must always be made between resolution and depth of field.

The ability for taking holograms from burning strands and 2-D slabs was demonstrated at different pressures. The laser power available with the present system was not enough to overcome the problems posed by the smoke and thermal cells when comparatively large amounts (slabs) of propellant or propellants with a high number of small aluminum particles were burned. The power density of the holographic system should be increased either by acquiring another laser source or by reducing the size of the existing beam through appropriate optics.

A speckle removal system (mylar disc) was used successfully for the reconstruction. The system presently has focusing problems when pictures are taken. Improvement of the focusing control and a camera without a focusing ground glass are required. However, if particle size distribution data are to be obtained in a reasonable amount of time, an automatic data acquisition system is a necessity.

A laser system using a photodiode as a photosensor was developed for acquiring the volume-surface mean diameter

(D_{32}) of the exhaust particles of a small motor, by means of the diffractively scattered light method. The system was calibrated and successfully applied to the exhaust gases of a small solid propellant motor. The technique could be improved by employing slower scanning of the illumination profile of the scattered light. This would provide more accurate data readings. Initial results indicate that a proper calibration curve ($I(\theta)$ versus (θ)) obtained from particle size distributions of the same range as the expected exhaust particle sizes should be employed instead of the "universal" illumination profile curve. This result requires further verification.

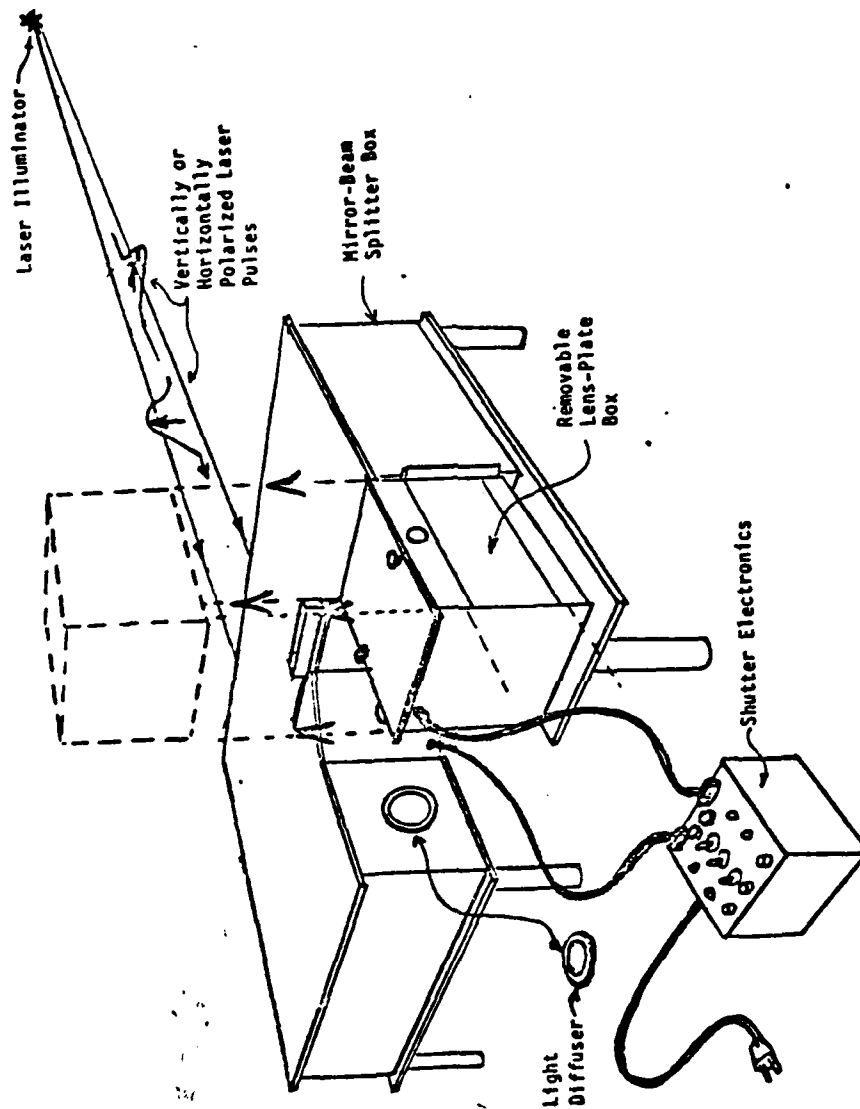


Fig. 20. Sketch of RPL Holocamera
(Adapted from Ref. 45)

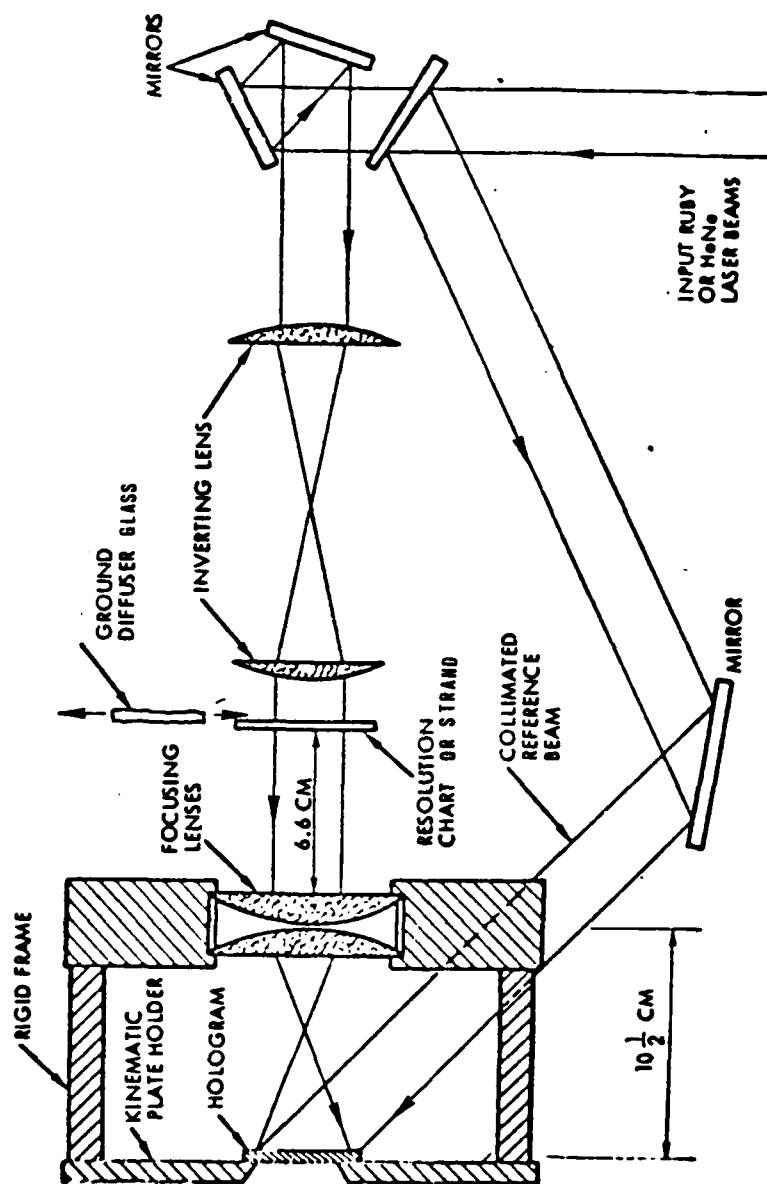


Fig. 21. Schematic of Two-beam Lens-assisted Holographic Arrangement
(Adapted from Ref. 45)

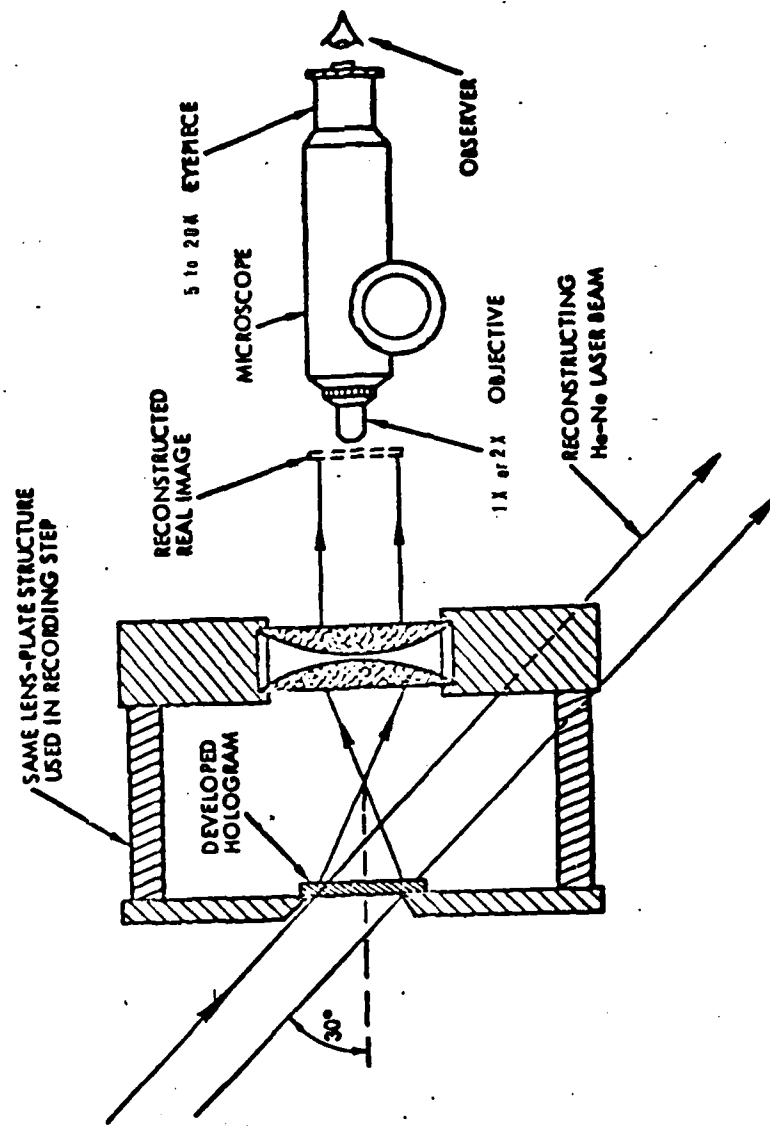


Fig. 22. Schematic of Hologram Reconstruction Method (Adapted from Ref. 45)



Fig. 23. Photographs of RPL Ruby Laser Components



Fig. 24. Photograph of the Hologram Reconstruction Apparatus

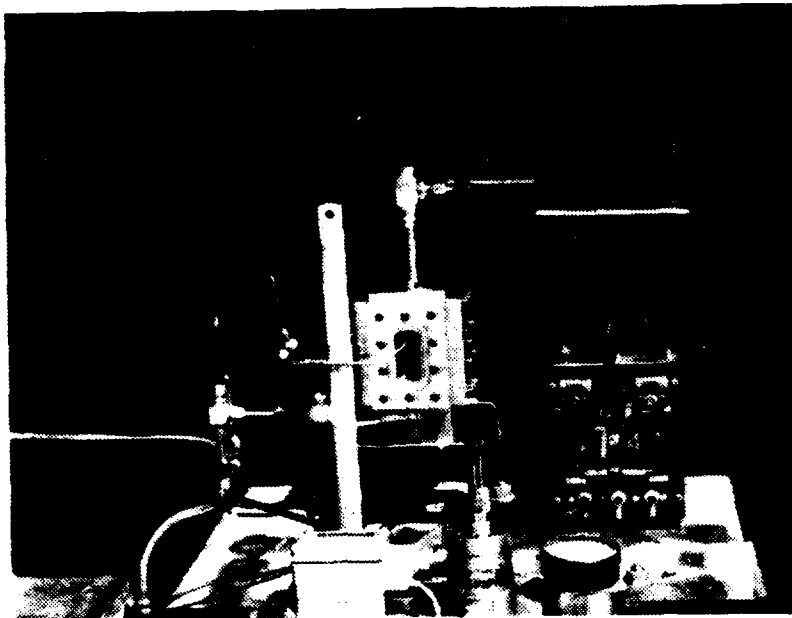


Fig. 25. Photograph of 2-D Motor with Control Box and Holocamera

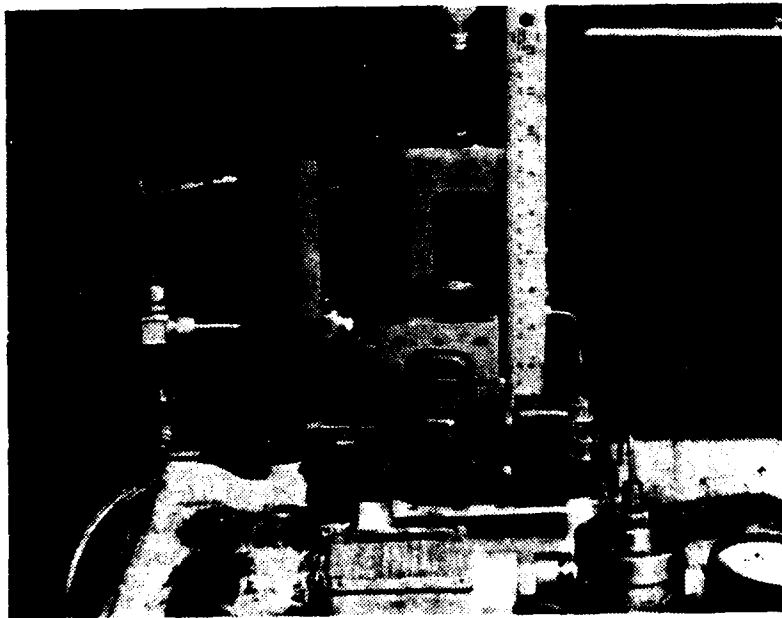


Fig. 26. Photograph of 2-D Motor Components

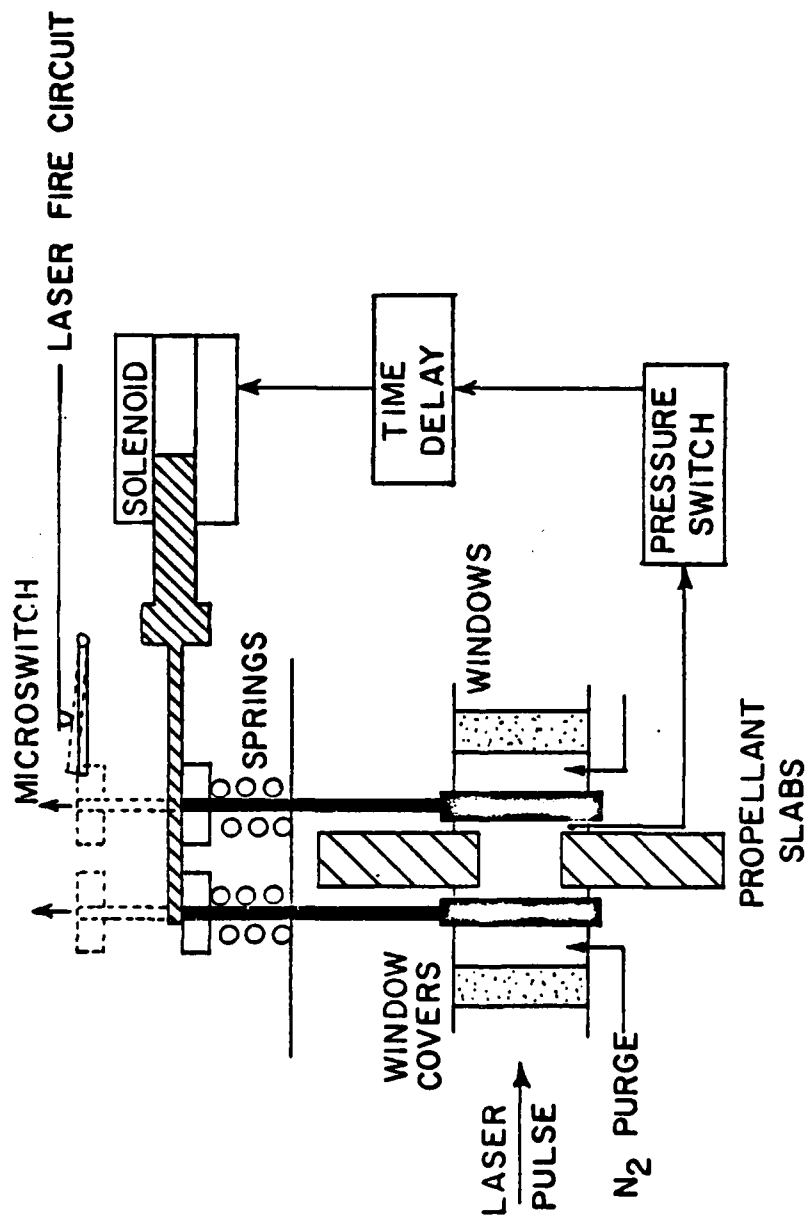
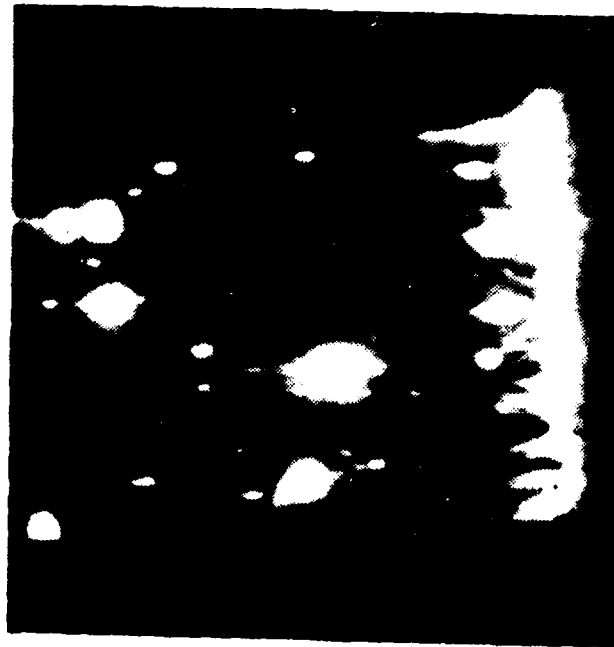


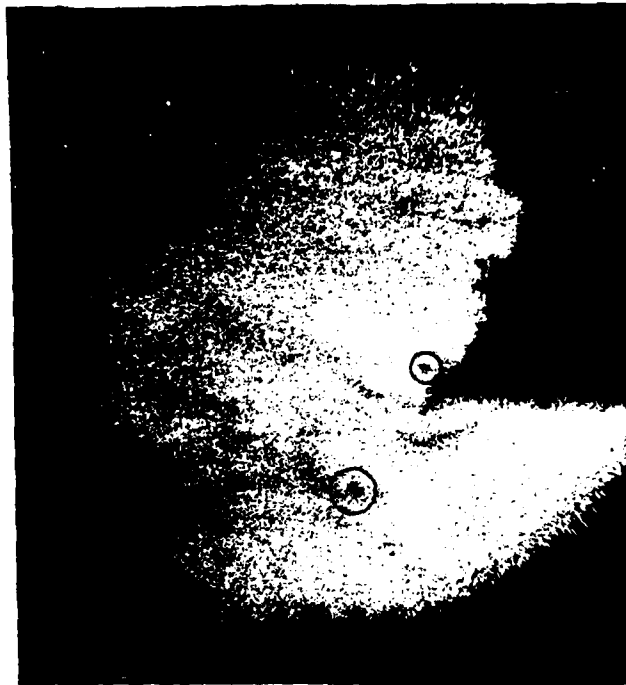
Fig. 27. Schematic of 2-D Motor Holographic Apparatus



Fig. 28. Hologram of 1951 USAF Resolution Target



Motion Picture; Scale 2800 $\mu\text{m}/\text{inch}$



Hologram, 50 μsec pulse, 28 ND filter;
Scale 1443 $\mu\text{m}/\text{inc}$

Fig. 29. WGS-5A Propellant Burned at 500 psi



(a) Hologram without
mylar disc;
scale 1443 $\mu\text{m}/\text{in}$.



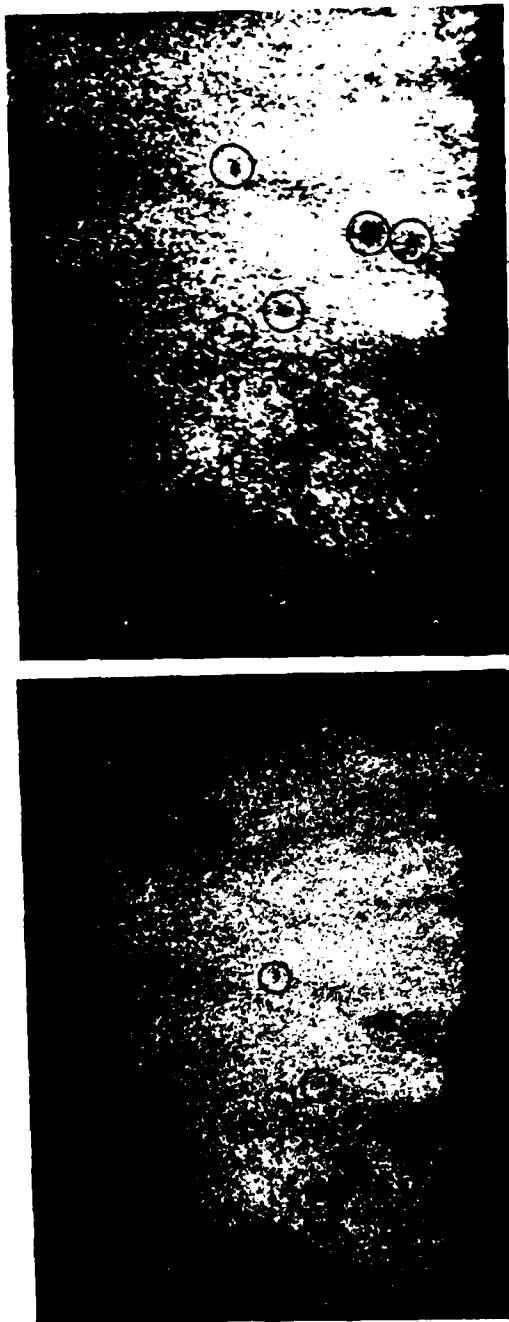
(b) Hologram with
mylar disc;
scale 1084 $\mu\text{m}/\text{in}$.

50 μsec pulse , .28 ND filter



(c) motion picture; scale 2800 $\mu\text{m}/\text{in}$.

Fig. 30. WGS-5A Propellant Burned at 1000 psi



50 μ sec pulse , .28 ND filter

(a) Hologram
without mylar disc;
scale 1445 μ m/in.

(b) Hologram
with mylar disc;
scale 1084 μ m/in.



(c) motion picture; scale 2800 μ m/in.

Fig. 31. WGS-6A Propellant Burned at 500 psi



(a) Motion Picture, scale 2800 $\mu\text{m}/\text{in.}$



(b) Hologram, 50 μsec pulse, .35 ND filter;
scale 1445 $\mu\text{m}/\text{in.}$

Fig. 32. WGS-6A Propellant Burned at 1000 psi

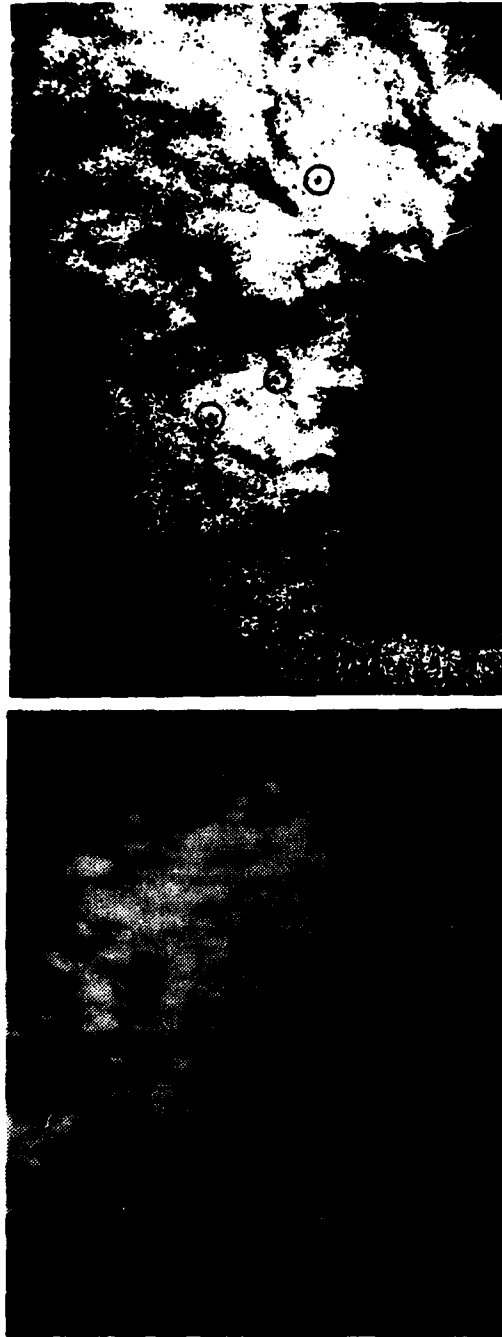


(a) Motion Picture; Scale 2800 $\mu\text{m}/\text{in}$.



(b) Hologram, 50 μsec pulse, .28 ND filter;
Scale 1443 $\mu\text{m}/\text{in}$.

Fig. 33. WGS-7A Propellant Burned at 500 psi



(a) Motion Picture; Scale 2800 $\mu\text{m}/\text{in.}$ (b) Hologram; 50 μsec pulse.
.35 ND filter; Scale 1443 $\mu\text{m}/\text{in.}$

Fig. 34. WGS-7A Propellant Burned at 1000 psi

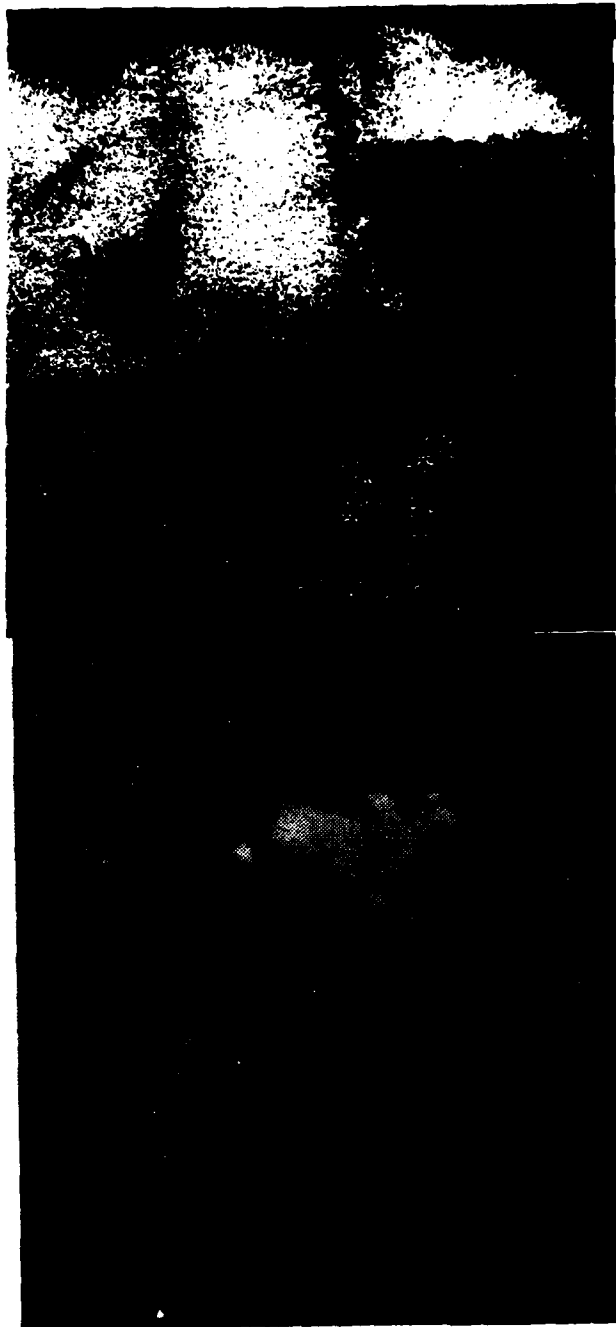


(a) 500 psi; .28 ND filter;
Scale 1084 $\mu\text{m}/\text{in}.$



(b) 1000 psi; .35 ND filter;
Scale 1443 $\mu\text{m}/\text{in}.$

Fig. 35. N-7 Propellant Holograms
50 μsec Pulse



(a) Motion Picture; Scale 2800 $\mu\text{m}/\text{in.}$ (b) Hologram; 50 μsec pulse, .35 ND filter; Scale 1084 $\mu\text{m}/\text{in.}$

Fig. 36. WGS-7 Propellant Burned at 1000 psi

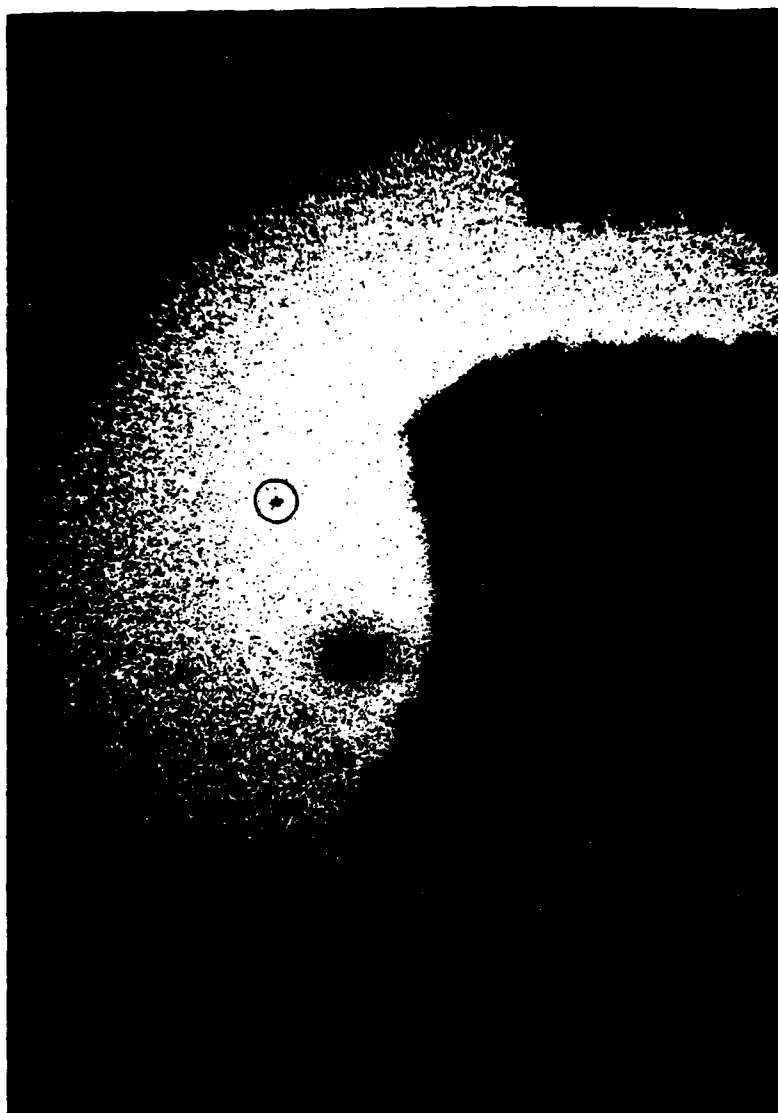


Fig. 37. Hologram of WGS-5A Propellant Burned at Atmospheric Pressure, 10 μ sec Pulse, No ND Filter: Scale 1443 μ m/in

REFERENCES

1. Price, E. W., Sigman, R. K. and Sambamurthi, J. K., "Behavior of Aluminum in Solid Propellant Combustion", 1977, Georgian Institute of Technology, Atlanta, GA, AFOSR-TR-0468.
2. Geisler, R. L., "Summary Report on 1977 JANNAF Aluminum Combustion Workshop", held at Hercules, Inc., 10-11 May 1977, Magna, UT.
3. Caveny, L. H., and Gamy, A., "Aluminum Combustion under Rocket Motor Conditions", AGARD Propulsion and Energetics Panel Symposium on Solid Rocket Motor Technology, 2-5 April 1979, Oslo, Norway.
4. Coats, D. E., et al, "A Computer Program for the Prediction of Solid Propellant Rocket Motor Performance, "Volume I, AFRPL-TR-75-36, Ultra Systems, Inc., July 1975.
5. Hermesen, R. W., "Aluminum Oxide Particle Size for Solid Rocket Motor Performance Prediction", AIAA-81-0035, AIAA 19th Aerospace Sciences Meeting, 12-15 January 1981.
6. Cohen, N. S., "Composite Burn Rate Modeling", AGARD Conference Proceedings No. 259, "Solid Rocket Motor Technology", (AGARD-CP-259), June 1979.
7. Derr, R. L., Churchill, H. L. and Fleming, R. W., "Aluminum Behavior in Solid Propellant Combustion", AFRPL-TR-74-13, AFRPL, Edwards, CA, May 1974.
8. Barrere, U., "Recent Experimental Results on the Combustion of Aluminum and Other Metals", Proceedings of AGARD Meeting on the Reactions of Gases and Solids, October 1969.
9. Gany, A., Caveny, L. H. and Summerfield, N., "Aluminized Solid Propellants Burning in a Rocket Motor Flow Field", AIAA Journal, Vol. 16, No. 7, July 1978, pp. 736-739.
10. Caveny, L. H. and Gany, A., "Breakup of Al/AlO_3 Agglomerates in Accelerating Flow Fields", AIAA Paper No. 79-0300, AIAA Aerospace Science Meeting, January 1979.
11. Geisler, R. L., Kinkead, S. A. and Bekcman, C. W., "The Relationship Between Solid Propellant Formulation Variables and Motor Performance", AIAA Paper No. 75-1199, October 1975, AIAA/SAE 11th Propulsion Conference, Anaheim, CA.

12. Micheli, P. L. and Schmidt, W. G., "Behavior of Aluminum in Solid Rocket Motors", Report AFRPL-TR-77-29, Aerojet Solid Propulsion Company, Sacramento, CA, December 1977.
13. George, D., "Recent Advances in Solid Rockets Motor Performance Prediction Capability", AIAA Paper No. 81-0033, AIAA 19th Aerospace Sciences Meeting, 12-15 January 1981, St. Louis, MO.
14. Gany, A. and Caveny, L. H., "Agglomeration and Ignition Mechanism of Aluminum Particles in Solid Propellants", Proceedings of the 17th International Symposium on Combustion, August 1978.
15. Hunter, S. C., et al, "Gas-Particle Nozzle Flows with Reaction and Particle Size Change", AIAA Paper No. 81-0037, AIAA 19th Aerospace Sciences Meeting, 12-15 January 1981.
16. Nejad, A. S., Schetz, J. A. and Jakubowski, A. K., "Mean Droplet Diameter Resulting from Atomization of a Transverse Liquid Jet in a Supersonic Air Stream", AFOSR-TR-79-0004, November 1978.
17. Diloreto, V. D., "An Experimental Study of Solid Propellant Deflagration Using High Speed Motion Pictures and Postfire Residue Analysis", Master Science thesis, Naval Postgraduate School, June 1980.
18. Boggs, T. L., et al, "Cinephotomicrography and Scanning Electron Microscopy as Used to Study Solid Propellant Combustion at the Naval Weapons Center", NWC TP5944, May 1977.
19. "High Speed Photography, Kodak Publ. G-44.
20. Kreutle, K. J., "Applications of Particle Size Analysis in Combustion Research", AIAA Paper No. 77-978, July 1977.
21. Gumprecht, R. O. and Sliepcevich, C. M., "Scattering of Light by Large Spherical Particles", Journal of Phys. Chem. No. 57, 1953.
22. Chin, J. H., Sliepcevich, C. M. and Tribus, M., "Particle Size Distribution in Polydispersed Systems by Means of Measurements of Angular Variation of Intensity of Forward-Scattered Light at Very Small Angles", Journal of Phys. Chem, No. 59, 1955.

23. Dobbins, R. A., Crocco, L. and Glassman, I., "Measurement of Mean Particle Sizes of Sprays from Diffractively Scattered Light", AIAA Journal, Vol. 1, No. 8, 1963.
24. Muggels, R. A. and Evans, H. D., "Droplet Size Distribution in Sprays", Ind. Eng. Chem. 43, 1951.
25. Roberts, J. H. and Webb, M. J., "Measurements of Droplet Size for Wide Range Particle Distributions", AIAA Journal, Vol. 2, No. 3, 1964.
26. Dobbins, R. A. and Jizmagian, G. S., "Optical Scattering Cross Sections for Polydispersions of Dielectric Spheres", Journal of the Optical Society of America, Vol. 56, No. 10, 1966.
27. Dobbins, R. A. and Jizmagian, G. S., "Particle Size Measurements Based on Use of Mean Scattering Cross Sections", Journal of the Optical Society of America, Vol. 56, No. 10, 1966.
28. Hodgkinson, J. R., "Particle Sizing by Means of the Forward Scattering Lobe", Applied Optics, Vol. 5, No. 5, 1966.
29. Powell, E. A., Cassanova, R. A., Bankston, C. P. and Zinn, B. I., "Combustion Generated Smoke Diagnostics by Means of Optical Measurement Techniques", AIAA 14th Aerospace Sciences Meeting, January 1976, AIAA Paper No. 76-67.
30. Cashdollar, K. L., Calvin, K. L. and Singer, J. M., "Three-Wavelength Light Transmission Technique to Measure Smoke Particle Size and Concentration", Applied Optics, Vol. 18, No. 11, 1979.
31. Essawy, M. E. and Delfour, A. G., "Determining Size Distribution of Liquid Nitrogen Particles Flowing in an Airstream by Scattered Light Detection", AIAA Journal, Vol. 18, No. 6, 1980.
32. Van de Hulst, H. C., "Light-Scattering by Small Particles", John Wiley and Sons, Inc., NY, 1957.
33. Minnacet, M., "Light and Colors in the Open Air", Dover Publications, Inc., NY, 1961.
34. Ellison, J. M. K., Proc. Phys. Soc. (London), Sec. B, 70, 102, 1957.
35. Vonk, V., Ph.D. Thesis, University of London, 1948.

36. Plass, Gilbert N., "Mie Scattering and Absorption Cross Sections for Absorbing Particles", Applied Optics, Vol. 3, No. 7, July 1964.
37. Plass, G. N., "Temperature Dependence of the Mie Scattering and Absorption Cross Sections for Aluminum Oxide", Applied Optics, Vol. 4, No. 12, December 1965.
38. Plass, G. N., "Mie Scattering and Absorption Cross Sections for Absorbing Particles", Applied Optics, Vol. 5, No. 2, February 1966.
39. Asano, Shoji, "Light Scattering Properties of Spheroidal Particles", Applied Optics, Vol. 18, No. 5, 1 March 1979.
40. Wang, D. S., et al, "Light Scattering by Polydisperse Suspensions of Inhomogeneous Non-spherical Particles", Applied Optics, Vol. 18, No. 15, August 1979.
41. Melles-Griot, "He-Ne Laser Guide".
42. CRC, "Handbook of Chemistry and Physics", 59th Edition, 1978-1979.
43. Holve, Don and Self, S. A., "Optical Particle Sizing for in Situ Measurements", Part 1 and Part 2, Applied Optics, Vol. 18, No. 10, 15 May 1979.
44. Yu Francis, T. S., "Introduction to Diffraction, Information Processing, and Holography", The MIT Press.
45. Briones, R. A., Heflinger, L. O. and Wuerker, R. F., "Holographic Microscopy", Applied Optics, Vol. 17, No. 6, 15 March 1978.
46. Klein, N. and Dewilde, M. A., "Pulsed Holography for Combustion Diagnostics", CPIA Publication 329, November 1980.
47. Thompson, B. J., et al, "Application of Hologram Techniques for Particle Size Analysis", Applied Optics, Vol. 6, No. 3, March 1967.
48. Collier, R. J., et al, "Optical Holography", Academic Press, New York, 1971.
49. Heflinger, L. O., et al, "Holographic Motion Pictures of Microscopic Plankton", Applied Optics, Vol. 17, No. 6, 15 March 1978.

50. Soares, O. D. D., "Hologram Repositioning by an Interferometric Technique", Applied Optics, Vol. 18, No. 22, 15 November 1979.
51. Trolinger, J. D. and Heap, U. P., "Coal Particle Combustion Studied by Holography", Applied Optics, Vol. 18, No. 11, 1 June 1979.
52. Ewan, B. C. R., "Fraunhofer Plane Analysis of Particle Field Holograms", Applied Optics, Vol. 19, No. 8, 15 April 1980.
53. Wuerker, R. F. and Briones, R. A., "Operation Manual for Lens-Assisted Multipulse Holocamera with Reflected Light Option", AFRPL-TM-78-12, July 1978.
54. Briones, R. A. and Wuerker, R. F., "Instruction Manual for the Improved Ruby Laser Holographic Illuminator", AFRPL-TM-78-11, July 1978.

INITIAL DISTRIBUTION LISTS

	No. Copies
1. Defense Technical Information Center Cameron Station Alexandria, Virginia 22314	2
2. Library, Code 0142 Naval Postgraduate School Monterey, California 93940	2
3. Department Chairman, Code 67 Department of Aeronautics Naval Postgraduate School Monterey, California 93940	1
4. Professor D. W. Netzer Code 67Nt Department of Aeronautics Naval Postgraduate School Monterey, California 93940	3
5. Distinguished Professor A. E. Fuhs Code 67Fu Department of Aeronautics Naval Postgraduate School Monterey, California 93940	1
6. Hellenic Air Force Research and Technology Center (KETA) Delta Phaleron, Phaleron, Greece	1
7. Major S. G. Karagounis, HAF 1 Ischomachou Street Larissa, Greece	5